공학박사 학위논문

Synthesis and Morphology Control of Plasmonic Nanostructures for Optical Amplification *via* Seed-mediated Growth Approach

씨앗-매개 성장을 활용한 플라즈모닉 나노구조체 형태 제어와 광학 신호 증폭

2020년 2월

서울대학교 대학원

재료공학부

이윤영

Abstract

Synthesis and Morphology Control of Plasmonic Nanostructures for Optical Amplification *via* Seed-mediated Growth Approach

Yoon Young Lee

Department of Materials Science and Engineering

The Graduate School

Seoul National University

It is very important to control the morphology of the metal nanostructures because the structures of the nanoparticles are directly related to their optical properties. This change in optical characteristics of metal nanostructures is due to the plasmonic effect. Surface plasmon refers to a phenomenon in which electrons on the surface of a metal thin film are collectively oscillated by an electric field. When the size of the metal structure becomes nano-size smaller than the wavelength of the incident light, unlike the thin film, the plasmon does not move but is bound and oscillated in the structure. The frequency of this oscillation is different from that of bulk, so it looks different in our eyes and varies with the size and shape of the structure. This phenomenon is called localized surface plasmon

resonance(LSPR). Due to this LSPR phenomenon, the resonant wavelength band of a metal such as gold or silver is located in the visible wavelength region, thus various absorption spectra are displayed in the visible region according to the shape of the gold or silver nanostructure. In addition, the electromagnetic field can be amplified in the vicinity of the plasmonic nanostructure, and the closer to the structure, the larger the electromagnetic signal. These interesting optical and application properties have led to a lot of efforts to control the shape of nanostructures. Seed-mediated growth synthetic method is a representative plasmonic nanostructure fabrication method of the bottom-up approach, which is effective to control the size and shape of the structure by separating the nucleation step and the growth step. Various shaped nanostructures have been reported using this approach, but the method and the shape obtainable are limited. Through this study, we tried to go beyond the limitations of conventional nanostructure fabrication. Herein, we investigated new methods to synthesize plasmonic nanoparticles with novel morphology, created unprecedented structure, and evaluated the optical properties of newly produced materials. First, a new synthesis method was used to control the growth of nanoparticles by adding organic thiol molecules to the seed mediated growth of gold nanoparticles. Generally, organic thiol molecules are used to introduce functional groups on the surface of nanoparticles and to assemble them. In this thesis, we studied the new role of organic thiol molecules in morphology control and produced new nanoparticles that have not been reported previously with unique morphology and optical

properties. In addition, the nucleic acid molecules were introduced into the seed-mediated growth synthesis process of gold nanoparticles to prepare chiral nanostructures and to control the properties of chiral nanoparticles previously reported. Since the pentose sugar in the nucleic acid molecule contains chiral carbons and the base in the nucleic acid molecule can interact with the gold surface, new chiral gold nanoparticles have been synthesized that effectively combine the structural properties of the nucleic acid molecule with the optical properties of the gold nanoparticles. In particular, according to the nucleotide sequence of the single-stranded DNA, it was confirmed that the chirality of the synthesized nanoparticles are variously changed. This means that by using a variety of patterned nucleic acid sequences through sophisticated programming in the nanostructure synthesis process, the chirality of the resulting nanoparticles can be variously controlled and enhanced.

Keywords: plasmon, nanoparticle, morphology, Raman scattering, chirality, nucleic acid

Student Number: 2014-21431

Contents

List of Tables

List of Figures

.

Chapter 1. Introduction

1.1 Structure-related optical property

In the field of research of optical materials, controlling the structure is one of the effective ways to achieve the desired optical properties. We can easily find structure-related optical properties in nature. For example, figure 1.1shows a jewel scarab beetle Chrysina gloriosa that is commonly found in montane juniper forests of the extreme southwestern United States and northern Mexico.[1] These scarab beetles have the property of changing their color according to the direction of light. When the light goes straight, it vibrates and extends in all directions. Among them, the light that moves in a spiral while drawing a circle is called circularly polarized light. These circularly polarized lights consist of 2 perpendicular waves of equal amplitude which are phase shifted by 90 degrees, resulting in the vectors rotating in either a clockwise or counterclockwise direction when looking into the direction of propagation of the light. We call circularly polarized light with counterclockwise direction a left-handed circularly polarized light(LCP) and the clockwise direction right-handed circularly polarized light (RCP). Chrysina gloriosa beetles appear green in color similar to leaves when LCP is irradiated. In contrast, under RCP, they do not show any particular color change. This unique optical property has been studied as the only means of communication for jewel scarab beetles that avoid predators. Also, the reason they show different colors

depending on the direction of polarization state of the incident light is the presence of spiral nanostructures encircling the left side of the shell. This helical structure has the property of selectively reflecting only circularly polarized light in the identical direction. As can be observed in nature, the structure of optical materials is very important because they can determine how they react to incident light. Thus, precise control of the structures of nanomaterials is critical for the desired optical properties.

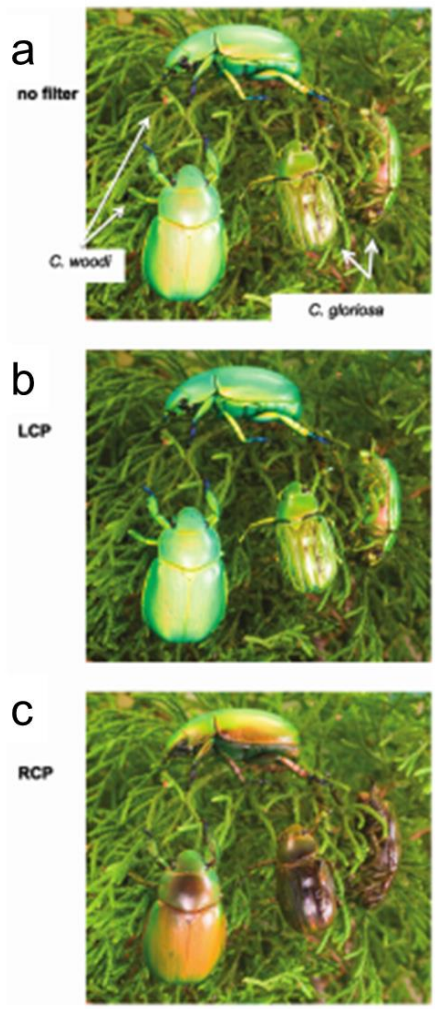

Figure 1.1 Images of Chrysina gloriosa jewel beetles on juniper branches, with (A) no filter and (B) left-handed circularly polarized light filters and (C) right-handed circularly polarized light filters.

1.2 Localized surface plasmon resonance and plasmonic nanostructures

The two cups shown in figure 1.2a look different, but they are actually the same cup. This cup which normally looked cloudy green, glows ruby red when illuminated from the inside. The cup is called Lycurgus Cup, one of the artifacts of ancient 4th century Rome. Figure 1.2b shows the stained glass of the Notre Dame Cathedral, one of Europe's most famous artifacts. Due to the medieval Gothic influence, cathedrals with a lot of large windows were built, and the stained glasses were created to illuminate the interior of the cathedral with the various colorful lights. The mysterious artifact created hundreds of years ago hides the secret of the interaction between metal nanoparticles and light. When metals such as gold and silver are reduced in size to nanoscale, they are found to have unique optical properties that are completely different from those in bulk. For example, blue light in stained glass is represented by spherical silver nanoparticles about 40 nanometers in size. (figure 1.3)[2]

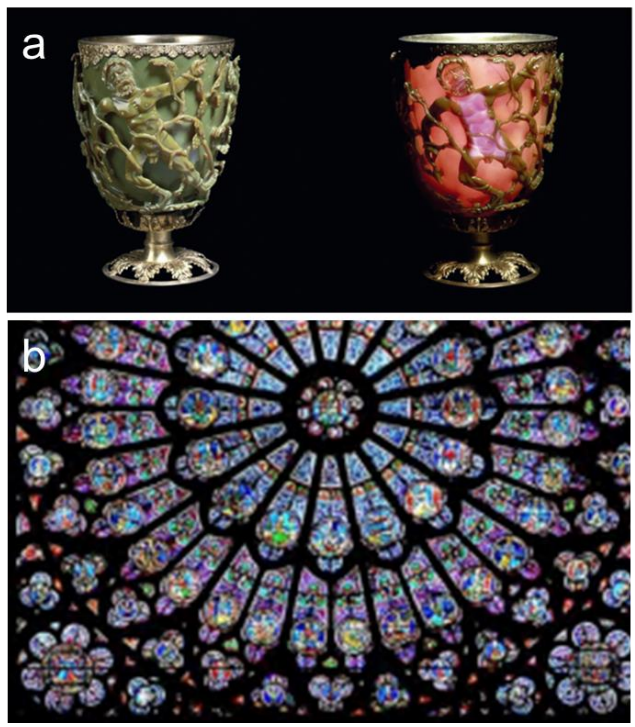

Figure 1.2 (a) Lycurgus cup, one of the artifacts of ancient 4th century Rome, which normally looked cloudy green, glows ruby red when illuminated from the inside. (b) The stained glass of the Notre Dame Cathedral, one of Europe's most famous artifacts.

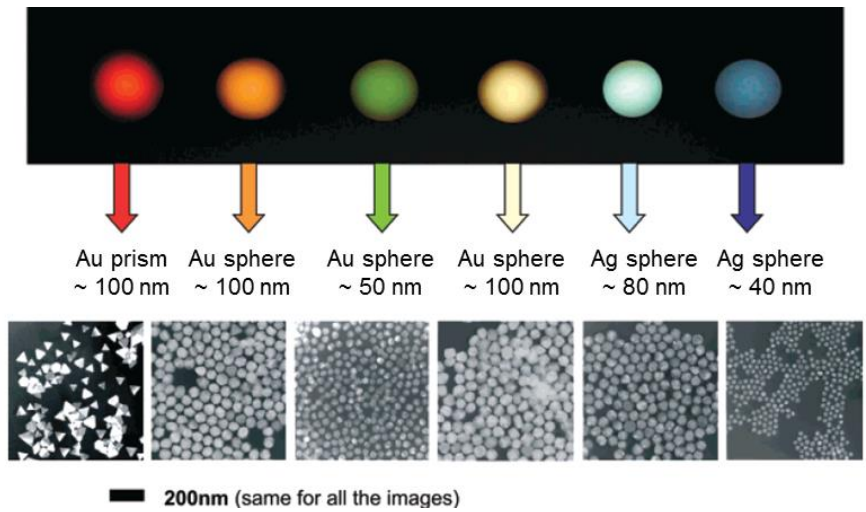

Figure 1.3 Sizes, shapes, and compositions of metal nanoparticles can be varied to create materials with distinct optical properties.

This change in the optical properties of the metal depending on the geometry is due to the localized surface plasmon resonance (LSPR) phenomenon in the nanoparticles. Surface plasmon refers to a phenomenon in which electrons on the surface of a metal thin film are collectively oscillated by an electric field.[3,4] Here, surface plasmon waves are generated and propagate at regular intervals along the interface.(Figure 1.4a)When the size of the metal structure becomes nano-size smaller than the wavelength of the incident light, unlike the thin film, the plasmon does not move but is bound and oscillated in the structure. The frequency of this oscillation is different from that of bulk, so it looks different in our eyes and varies with the size and shape of the structure. This phenomenon is called localized surface plasmon resonance (LSPR).(Figure 1.4b) Due to this LSPR phenomenon, the resonant wavelength band of a metal such as gold or silver is located in the visible wavelength region, thus various absorption spectra are displayed in the visible region according to the shape of the gold or silver nanostructure. (Figure 1.4c)[5] In addition, the electromagnetic field can be amplified in the vicinity of the plasmonic nanostructure, and the closer to the structure, the larger the electromagnetic signal. Here plasmonic ‘hot spot' is a term that refers to particularly large field amplification, mainly in the gaps, crevices, or sharp vertices of plasmonic materials. (Figure 1.5)[6-8]

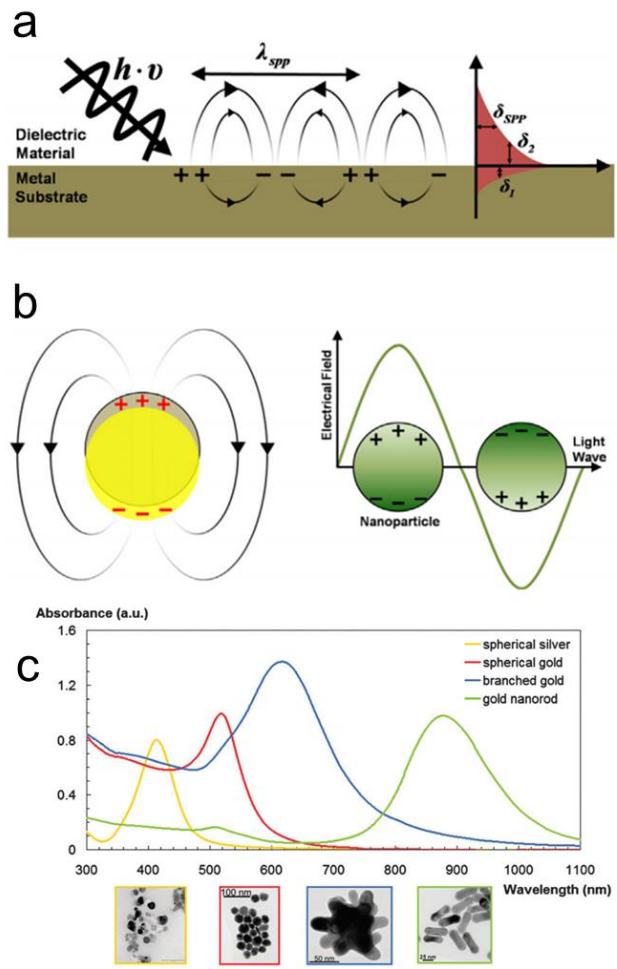

Figure 1.4 (a) Surface plasmon propagation wave in metal thin film. (b) Localized surface plasmon resonance (LSPR) phenomenon in metal nanoparticles. This occurs when the particle size is smaller than the wavelength of the incident wave. (c) Absorbance spectra of metal nanostructures. The LSPR of metal nanostructure is dependent on the size, shape and material.

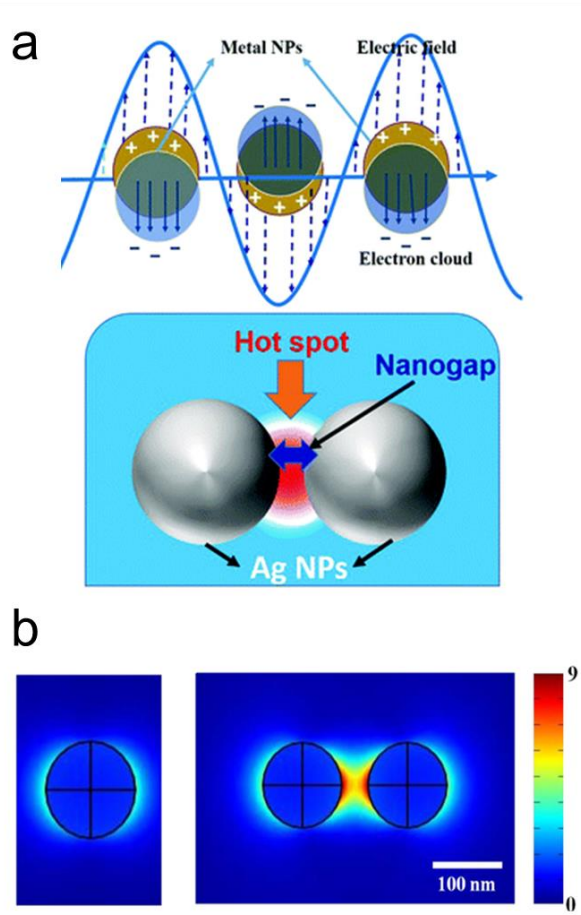

Figure 1.5 (a) Schematic of localized surface plasmons in metal nanostructure in an external electric field and plasmonic hotspot in the nanogap between silver nanoparticles. (b) Electric field distributions at a single Au nanoparticle (left panel) and nanoparticle dimer.

1.3 Seed-mediated growth approach for plasmonic nanostructures

In general, methods for manufacturing metal nanostructures and controlling their shape include top-down approaches, such as lithography, and bottom-up approaches, that gradually increase in size from atomic units. The metal ion reduction method is a representative method of the bottom-up approaches. When metal ions are reduced by using a reducing agent, the reduced atoms gather to form particles. This method was first reported by Turkevich in 1951, which produced nanoparticles of about 20 nm in size by reducing the aqueous gold ions with citric acid.(figure 1.6a)[9,10] Since then, various metal ion reduction methods have been reported to improve a wide size distribution and efficiently obtain nanoparticles of a desired size and shape. In the 2000s, seed-mediated growth synthesis was reported.[11,12] This approach is characterized by separating the nucleation and growth stages. Firstly, very small 5 nanometer seed particles are synthesized and grown again in the growth solution. (figure 1.6b) This method is one of the most widely used synthesis methods because it is effective in controlling the structure and size of the final product according to various synthesis conditions such as concentration, temperature, and pH change of growth solution components.[13]

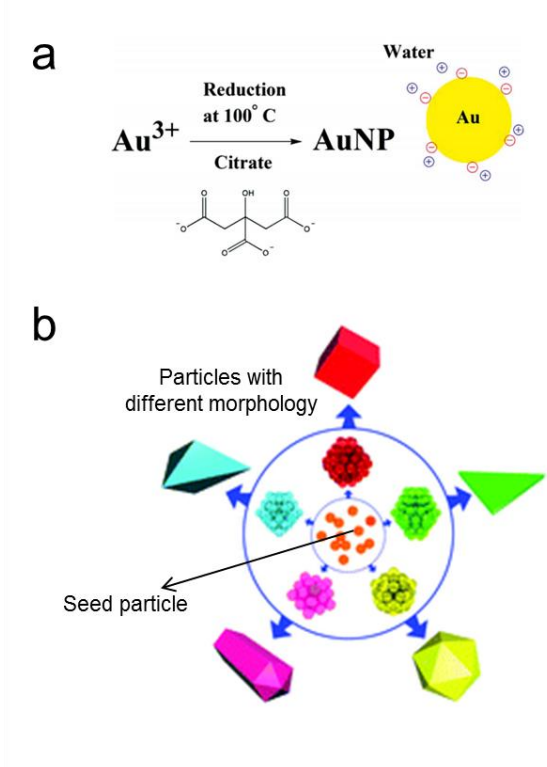

Figure 1.6 (a) Turkevich method for gold nanoparticle fabrication (b) Schematic of seed-mediated growth approach for nanoparticle synthesis

1.4 Plasmonic nanostructures for optical sensing applications

Surface-enhanced Raman scattering applications

Raman spectroscopy is used to measure the vibrational spectrum of a molecule to study the structure of the molecule or for qualitative and quantitative analysis of materials. Raman spectroscopy is a series of chemical bar codes, discovered by Indian physicist C. V. Raman, who won the Nobel Prize in Physics in 1930.[14] When a light passes through a substance, some parts of the light are scattered and deviate from the direction of travel and travels in the other direction. In this case, the scattered light may have the identical energy but may have less or more energy than the original incident light. The process of scattering while maintaining the original energy of the scattered light is called Rayleigh scattering or elastic scattering.(Figure 1.7)[15] Not only does a substance absorb energy when it is illuminated, but sometimes molecules in a high energy state can release energy. This phenomenon is called anti-Stokes Raman scattering. Raman scattering corresponds to inelastic scattering.

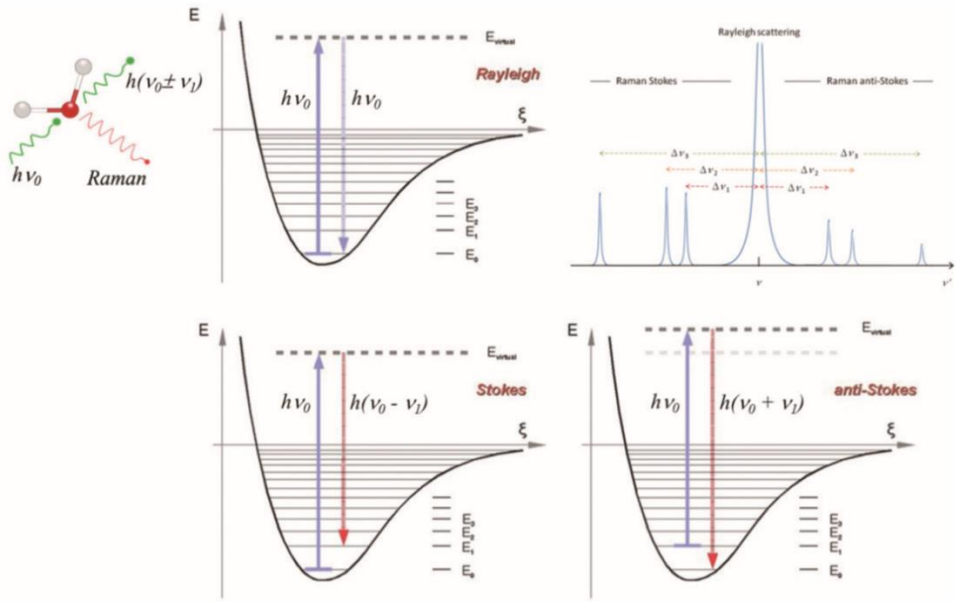

Figure 1.7 Schematic of Rayleigh scattering, Raman stokes scattering and Raman anti-stokes scattering

Raman scattering processes cannot directly measure vibrational energy as in infrared spectroscopy. Instead, vibration energy is measured by observing how much energy the scattered light has lost or gained compared to Rayleigh scattering. The spectrum shows how much the scattered light has shifted with respect to Rayleigh scattering as a Raman shift, which corresponds to the molecular vibration frequency. In addition to Raman scattering, fluorescence may occur when the biomaterial is irradiated with a laser in the visible region. The intensity of the fluorescence is very strong compared to the Raman scattering and occurs in a region similar to the region in which the Raman spectrum is measured, so the pure Raman spectrum cannot be obtained by covering the fluorescence peak. To solve this problem, using a light source with a wavelength that is too long to generate fluorescence can reduce the fluorescence interference and measure the Raman spectrum without the influence of fluorescence.

Despite many application values, one of the important reasons why Raman spectroscopy is not commercially available is the weak signal intensity. This is because the scattering cross section of Raman scattering spectroscopy is remarkably small compared to other spectroscopy. (Table.1.1)[16]

Type	Process	Cross-section(cm^2) of molecule
UV	Absorption	10^{-18}
IR	Absorption	10^{-21}
Fluorescence	Emission	10^{-19}
Rayleigh	Elastic scattering	10^{-26}
Raman	inelastic scattering	10^{-29}

Table 1.1 Comparison of cross section of molecules of Raman scattering and fluorescence emission

One of the ways to overcome this problem was reported in 1974 by Surface-enhanced Raman Scattering (SERS) by Fleishmann et al.[17] Surface-enhanced Raman scattering refers to a phenomenon in which the Raman signal of a molecule increases significantly when a target molecule is present in the vicinity of the metal nanostructure. They observed that the Raman signal increased by about 106 times when the pyridine molecules were adsorbed in aqueous solution after repeated oxidation-reduction on the silver electrode. When the incident laser collides with the metal nanostructure and the dielectric interface, if the frequency of the incident light coincides with the frequency of the free electrons of the metal, electromagnetic waves of the light may induce collective oscillation of the free electrons. This is called Surface Plasmon Resonance (SPR). SPR frequency depends on particle size, shape, dielectric environment, electron density, effective electron mass, and so on. In metal nanostructures, SPR can be highly localized at a specific location. This is called Localized SPR (LSPR) and this area is called hot-spots. The nanoparticles having such strong LSPR effects are called plasmonic nanoparticles, and include Ag, Au, and Cu. The SERS effect occurs when Raman active molecules are placed in hot-spots near the surface of the plasmonic nanostructures.

Chiroptical sensing applications

Nanobiosensors based on localized surface plasmon resonance (LSPR) phenomena track the shifts of resonance peaks in the extinction spectra with respect to the change of the surrounding medium near the plasmonic nanostructure.[18,19] For the enhanced LSPR sensitivity, number of approaches which utilize the shape-engineered materials composed of noble metals such as Au and Ag have been developed and recently several ideas employing chiral metamaterial platforms have been proposed.

Fischer and coworkers reported significant refractive index sensitivities by employing shape-engineered chiral plasmonic nanostructures. (Figure 1.8a)[20] They introduced the theoretical concepts, such as full width at half maximum (FWHM) and figure of merit (FOM) for improving the sensitivities in LSPR sensors with chiral platforms and illustrated the roles of chirality and properties of the materials. When theoretically obtaining the sensitivity (S_n) and FOM (S_n/FWHM) at the point where the CD value is zero, the term of 'chiral shape factor' is introduced. Higher FOM value could be obtained by applying ‘chiral shape factor’ with increased magnitude. Also it has been reported that the sensitivity can be improved by controlling the alloy composition with the metal having lower wavelength dependency of the dielectric constant.

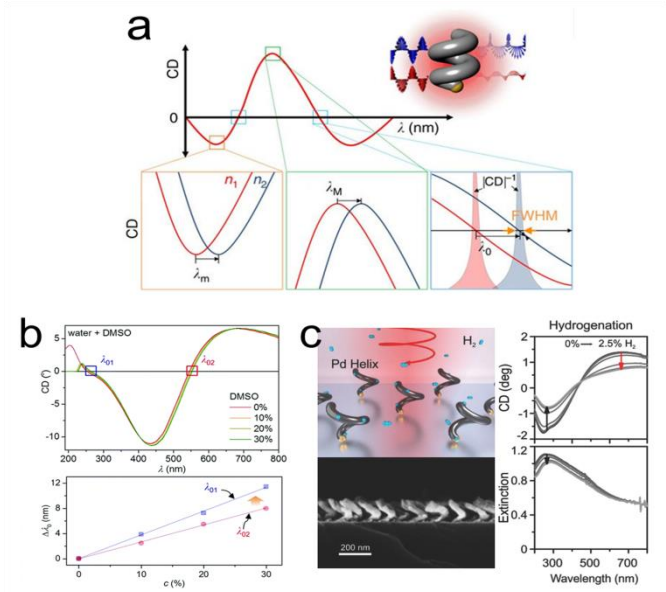

Figure 1.8 Representative examples of platforms for detection of changes in surrounding media (a) A schematic diagram of circular dichroism sensing using chiral plasmonic nanohelices. 3 bottom panels illustrate the resonance shift in the circular dichroism(CD) spectra at minimum, maximum and zero crossing wavelength where the refractive indices are changed between n_1 and n_2. (b) CD spectra of chiral magnesium nanoparticles in 4 different DMSO-water mixtures red : 0%, orange : 10%, yellow : 20% and green : 30%)(upper panel) Wavelength shift of the λ_{01} and λ_{02} as a function of DMSO concentration.(lower panel) (c) A schematic diagram of chiral plasmonic hydrogen sensor using Pd nanohelice (left, upper panel) Electron microscopy image of cross section of Pd nanohelice. (left, lower panel) CD and extinction spectra during hydrogenation and dehydrogenation (right panel) Arrows indicate the evolutions of the spectra with the hydrogen uptake.

A molecular LSPR sensor using chiral magnesium nanoparticles with notable chiroptical effects in the ultraviolet (UV) region was also reported.[21] The change in the refractive index of dimethyl sulfoxide (DMSO) solution caused by the change in concentration as a function of the wavelength (dn/dC), which is larger in UV region rather than the visible region. Figure 1.8b (upper panel) shows CD result of chiral Mg nanoparticles in DMSO-water mixtures ranging from 0% to 30%. As shown in Figure 1.8b (lower panel), the wavelength shift in the UV region is larger than that of shift in the visible region. The results show that the UV plasmonics is promising for enhanced LSPR sensors due to the dispersion of the medium. Liu and coworkers demonstrated a hydrogen sensing platform by employing chiral palladium nanomaterial with helical structures.[22] When exposed to hydrogen, Pd metal goes through a reversible phase transition to a metal hydride form and depends on the concentration. It is well known that the chiroptical properties of Pd nanostructure vary with the hydrogen uptake and depend on the concentration. As shown in figure 1.8c, CD and extinction intensities are decreased in response to the increasing hydrogen concentrations. When the hydrogen concentration increased to 1.6%, the CD signal change was about 40%, while the extinction signal change was only 10%. In addition, compared with the extinction spectra, the signal-to-noise of CD was higher and the CD signal change upon hydrogen uptake was observed in the broad wavelength range from ultraviolet to near infrared.

Metamaterials with chiral morphologies fabricated in various ways have been utilized for chiral enantiomer detection. The strong enhancement of near-field optical chirality in the vicinity of the metamaterial platforms can induce the sensitivity amplification. Figure 1.9a shows a SEM image of a planar chiral metamaterial (PCM) named 'gammadion'. The array structure with a gold gammadion of about 400 nm showed a strong CD signal around 800 nm.[23] PCMs were fabricated as left-handed and right-handed configuration and their CD spectra were observed as mirror images. It has been found that the enhancement of a large and uniform local optical chirality maximizes the molecular signal on the plasmonic gammadion structures. For example, in the presence of a protein tertiary structure (beta-lactoglobulin), the difference in resonance peak shifts between RCP and LCP light was observed, allowing the detection at pictogram level. In the case of achiral molecule (ethanol), the difference of peak shifts was zero.

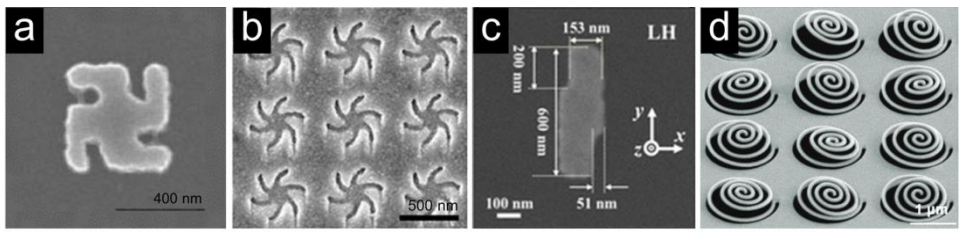

Figure 1.9 Representative examples of chiral metamaterial platforms for detection of molecular handedness: (a) a SEM image of the gold gammadion nanostructure, (b) a SEM image of the gold Shuriken nanostructure, (c) a SEM image of the left-handed enantiomer of the lightning-bolt like gold nanostructure, (d) a tilted SEM image of the as-fabricated chiral metasurface consisting of arrays of 3 dimensional Archimedean spirals

Figure 1.9b shows a SEM image of Shuriken-shaped plasmonic metafilm.[24] The left-handed or right-handed Shuriken structures have been reported to be suitable as probes for analysis of biointerface. Chiral near fields generated near this Shuriken structure are utilized to study the level of structural order. The chiroptical responses of the metamaterials are varied by the presence of a biomolecular protein layer and the magnitude of asymmetry depends on the structural order. Consequently, specifying a protein-protein interaction based on the level of structural anisotropy becomes available.[25,26] Large-area arrays of chiral plasmonic nanocrescents were fabricated using a colloidal lithography technique by adjusting the mutual deposition angle of gold and silica.[27] It was observed that the simulated optical chirality enhancement was maximized at the sharp tips of the plasmonicnanocrescents. Okamoto and coworkers prepared a two-dimensional lightning-bolt-like gold nanostructure consisting of two displaced rectangles and observed the enhancement in dissymmetry of circularly polarized photoluminescence. (Figure 1.9c)[28] The structures fabricated in both left-handed and right-handedness was used to provide a circularly polarized luminescence source, and a strong photoluminescence enhancement was observed in the 800 nm wavelength range.

In addition to the two-dimensional plasmonic asymmetric nanostructures described so far, structures with both plasmonic Fano resonance effects and strong optical chirality were also reported.[29,30] Cao and coworkers have introduced a gold chiral array of disc-double split ring resonators with dipole-octupole Fano resonance.[31] Using the distinct total transverse force and potential well from this structure, an effective enantioselective separation of sub-10 nm chiral particles can be achievable. Fang and coworkers fabricated 6-fold symmetric chiral heptamers and systematically studied the chiroptical response with changing the inter-particle rotation angles and separation distance. The authors noted the response greatly depends on the plasmonic Fano resonance effect. Later, further studies on this structure were conducted to study chirality at subnanoscale using cathodoluminescence microscopy and spectroscopy, which can carry the polarization information.[32,33]

Recently, efforts have been devoted to implement 3-dimensional plasmonic chiral metamaterial platforms. Compared to planar materials, 3D chiral metamaterials have the advantage of more uniform and broadband near-field optical chirality enhancement. Accordingly, enantiomer-specific molecular sensing with more uniform, sensitive, and wider wavelength ranges can be expected using 3D chiral metamaterials. However, it is still a challenging topic with many technical barriers in practical applications.

Including the planar and 3D metamaterials and geometrically chiral plasmonic platforms can exhibit far-field signals that are larger than natural chiral molecules, which can be a stumbling block detecting the chiroptical signal of the analyte molecules. The concept of 'plasmonic racemates' which combines the advantage of strong near-field optical response of chiral platforms with zero far-field optical response of achiral systems was proposed. Here each individual structure is chiral, while the whole array is an achiral platform in the presence of enantiomers. Quidant and coworkers reported a racemic nanoplasmonic array for the enantiomer detection. (Figure 1.10a)[34] Racemic gold nanoarrays consisting of gammadion structures were fabricated using an e-beam lithography. The designed sensor showed zero intrinsic CD, high optical chirality and electric field enhancement in the near-field. It has been utilized for distinguishing D-, L- and racemic forms of phenylalanine molecules. Valev and coworkers proposed a racemic metamaterial platform, consisting of equivalent quantities of opposite chiral unit cells. (Figure 1.10b)[35] They reported the numerical simulation results for diffraction circular intensity spectroscopy, yielding an intensity difference of up to 15% and suggested the potential use of racemic nanogratings in the hyper-sensitive chiral molecular detections.

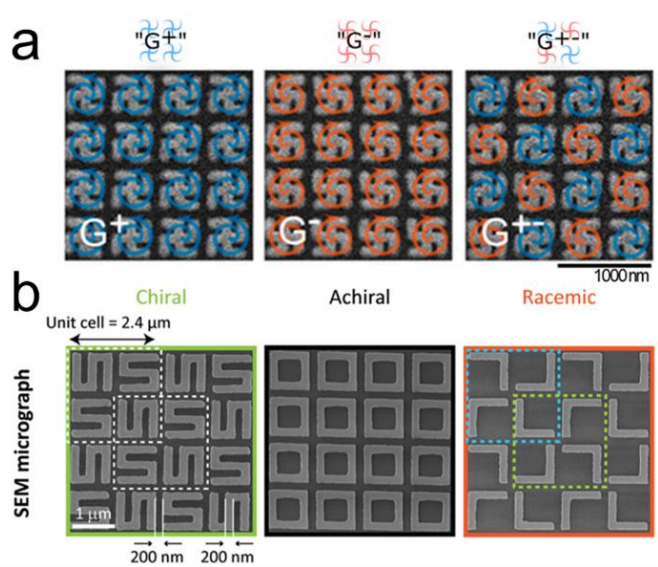

Figure 1.10 Representative examples of racemic metamaterial platforms for detection of molecular handedness. Racemic metamaterial platforms can keep large values of optical chirality and near-field enhancement and at the same time far-field CD intensity can be suppressed. (a) SEM images of handed(G+, G-) and racemic(G+-) gold gammadion arrays. (b) SEM image of S-shaped chiral chip is shown in the green box and the achiral chip design (black box) is made of square-rings and the racemic chip (orange box) consists of L-shaped structures. The cyan and green lined-boxes in the racemic sample indicate the two enantiomeric unit cells.

In addition to using optical chirality derived from the geometry of the plasmonic metamaterials, the utilization of chiral assemblies of the plasmonic nanostructures in the presence of the target molecules have also been reported.[36,37] Biomolecules can induce chiral arrangement of plasmonic nanostructures, giving rise to intense chiroptical responses at the plasmon resonance wavelength region.

A chiroplasmonic bioanalysis study using the gold-silver nanoparticle heterodimer is shown in figure 1.11a.[38] When bridged by biomolecules, the nanoparticle dimers formed a scissor-like geometry with long axes at an angle of 9 degrees and its CD response is generated in the visible region. This heterodimer structure can be used to detect biomarker molecules such as prostate-specific antigen. A DNA-based self -assembled core-satellite structure was also used to detect Ochratoxin A molecules. (figure 1.11b).[39] First, an aptamer of Ochratoxin A and a complementary sequence are coupled to the surfaces of gold nanoshells respectively. In the absence of Ochratoxin A, the core-satellite structure showed a strong CD response, while in the presence of Ochratoxin A, the coupling phenomenon of the nanostructures was decreased and the CD intensity was weakened as the concentration of the biomolecule is increased. Figure 1.11c shows a study of biomarker detection of Parkinson's disease by observing the chiral arrangement of plasmonic nanostructures.[40] The authors employed Au nanorodsto react in a different way to the stable monomeric proteins and the infectious fibrils. In the presence of monomeric proteins, Au nanorods did not show any chiroptical response. However, in the presence of amyloid fibrils, their helical properties

caused the nanorods to form a 3D chiral arrangement and exhibit CD response at the resonance wavelength. They noted that this detection method could also be applied to the human brain samples.

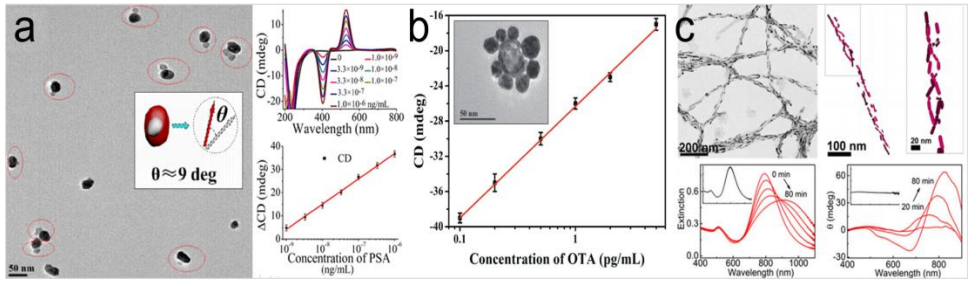

Figure 1.11 Representative examples of platforms for detection of molecules inducing self-assembled chiral structure (a) SEM image of gold-silver heterodimers bridged by immunocomplex.(left panel) When bridged by an antigen and antibody, the nanoparticle dimers display a scissor-like conformation with long axes at an angle of 9 degrees.(inset in left panel) Results of detection of PSA with NP heterodimers.(right panel) CD spectra with increasing concentrations of PSA solution (right, upper panel) CD calibration curves for PSA detection, where ΔCD is $CD_{530\ nm} - CD_{403\ nm}$, as a function of logarithmic PSA concentrations.(right, lower panel) (b) Plot of CD (at 521 nm) of shell core–Au satellite superstructures versus the different concentrations of ochratoxin A(0.1, 0.2, 0.5, 1, 2, or 5 pg /mL). Inset : A SEM image of a gold shell core-silver satellite assembly to detect mycotoxin ochratoxin A. (c) Chiral sensing for Parkinson's disease using arrangement of gold nanorods. TEM and cryo-TEM tomography images of gold nanorod-protein fiber composite(upper panel) and extinction and circular dichroism spectral changes after addition of fibrillar proteins. Insets : corresponding spectra when added monomeric proteins.(lower panel)

1.5 Scope of thesis

Seed-mediated growth approach is one of the most widely used synthesis methods because it is effective in controlling the structure and size of the final product according to various synthetic conditions. Based on our understanding of gold nanoparticle seed mediated growth synthesis, in this thesis, we used a strategy to introduce organic molecules into the growth process of nanoparticles to produce gold nanostructures with controlled morphology and to amplify optical responses. We have proposed a simple and highly applicable synthesis method, and the characteristics of the nanoparticles formed are programmably controlled according to the characteristics of the organic molecules used. In addition, the unique chirality of organic molecules is expressed in inorganic nano materials.

Chapter 2. Organothiol-assisted synthesis of gold nanoparticles for surface-enhanced Raman scattering (SERS) enhancement

2.1 Introduction

In the Surface-enhanced Raman scattering (SERS) spectroscopy has proven an attractive analytical tool owing to its ability to detect molecular species with high sensitivity, good photostability, and its large multiplex capacity.[41] Much effort has been devoted to the development of suitable plasmonic nanoparticles as probes for diverse SERS applications, such as molecular sensing, reaction monitoring, and biomedical diagnosis.[42-44] This effort has included fine-tuning of their sizes and morphologies which affects their optical properties determining the range of biological applications.[45-48]

Creating sharp edges or nanogaps in a plasmonic structure, which are called "hot spots", offers an efficient way to generate a strong SERS signal.[49,50] Nanoparticles with sharp edges or horns, such as nanostars, have been highlighted owing to their hot-spot-containing morphologies. However, it is difficult to control the size of such nanoparticles because their sizes tend to depend on the evolution process during synthesis, resulting in the different branching structures or levels of morphological development.[51] The use of

aggregates and assemblies of plasmonic nanoparticles to create nanogaps for hot spots has been shown to enhance the SERS properties.[52-58] The strong coupling of localized surface plasmons near the hot spots induces an increase of the localized field. In general, however, it is difficult to control the sizes, shapes, and signal uniformities of aggregates. In addition, owing to their relatively large sizes, applying aggregates in biosensors is not easily achievable.[59]

Single-particle-level SERS provides a way to address these limitations. Structures such as rough gold microspheres, bumpy silver nanoshells, and silver–gold core–shell satellite heterostructures have been designed as single-particle-detectable nanoprobes with highly enhanced SERS signals.[60-62] However, there are still challenges in the development of size-tunable SERS nanoprobes which have single-particle detectable sensitivity for broader bioapplications.

Herein, we describe a facile approach for the synthesis of gold nanocubes (Au NCs) with many bumps by controlled regrowth and simultaneous conjugation with organothiol molecules acting as Raman reporters. The newly synthesized gold bumpy nanocubes (Au BNCs) not only have the edges and corners of Au NCs, which generate enhanced localized fields,[63] but numerous hot spots are also located on the surfaces of a single nanoparticle. Therefore, Au BNCs provide high sensitivity and signal uniformity for single-particle-level SERS detection without the polarization-dependent signal fluctuation that has been observed in previous nanocube-based SERS substrates.[64] We expect this

new particle to be applicable to a variety of fields, including face-to-face particle assembly, plasmon-enhanced spectroscopy, and probes for biosensing applications owing to the following advantages: (i) maintenance of a cubic outline; (ii) high uniformity; and (iii) size-controllable synthesis by controlling the precursor concentration.

2.2 Synthesis of Au bumpy nanocubes

To synthesize size-controlled, monodisperse novel gold nanoparticles, we adopted a modified seed-mediated growth method. Au NCs (ca. 44 nm; Au NC_{44}) with high uniformity, generated by a well-known seed-mediated method, were incubated in a growth solution including 4-aminothiophenol (4-ATP), which is a well-known Raman reporter molecule and also operates as a morphological modifier (Figure 2.1). During the additional growth process, Au NCs with bumpy surfaces were grown. Their cube-like morphology was maintained, while their size varied depending on the precursor concentration.

Chemicals

$HAuCl_4 \cdot 3H_2O$ (99.9%), sodium borohydride ($NaBH_4$, 99%), CTAB (99%), 4-ATP (99%), and AA (99%) were purchased from Sigma-Aldrich and were used without further purification. Dimethyl sulfoxide (DMSO, 99.5%) was purchased from Daejung Chemicals. High-purity deionized (DI) water (18.2 MΩ cm) was used in all of the procedures.

Preparation of Au NCs

Au NCs with a 44 nm edge length were synthesized as previously reported.[65] First, small gold seeds (~2.5 nm) were prepared by the reduction of a $HAuCl_4 \cdot 3H_2O$ aqueous solution (10 mM, 250 μL) with a $NaBH_4$ aqueous solution (10 mM, 800 μL) in a CTAB aqueous solution (100 mM, 7.5 mL). The

gold seeds were added to the growth solution consisting of a $HAuCl_4 \cdot 3H_2O$ aqueous solution (10 mM, 0.2 mL), a CTAB aqueous solution (100 mM, 1.6 mL), and an AA aqueous solution (100 mM, 0.95 mL). After 15 min, the synthesized Au NCs with a 44 nm edge length were washed by centrifugation (10 000 rpm, 60 s) and dispersed in DI water.

Regrowth on Au NCs

A CTAB solution (100 mM, 0.8 mL) was added to 3.95 mL of DI water. $HAuCl_4 \cdot 3H_2O$ aqueous solutions of various concentrations, an AA aqueous solution (100 mM, 0.475 mL), and 4-ATP (5 mM in DMSO, 0.5 μL) were mixed into the CTAB solution. Regrowth on the Au NCs was started by the addition of the NCs, which were previously synthesized. After 2 h, the solution was centrifuged (5000 rpm, 60 s) to remove unreacted reagents.

Characterization

UV-visible extinction spectra of various sized Au NCs were obtained using an UV-visible spectrometer (NanoDrop 2000c, Thermo Scientific). The sizes, morphologies, and homogeneities of the Au NCs were analyzed using SEM (SUPRA 55VP, Carl Zeiss) and TEM (JEM1010, JEOL). The elemental analysis data was obtained by energy-dispersive X-ray spectroscopy (EDX) with SEM (JEOL JSM-6360). The SERS spectra of the Au NCs were obtained using a confocal Raman microscope (LabRam 300, JY-Horiba). The Raman scattered light for each Au NC was collected in a 180° back-scattering geometry and

detected using a spectrometer equipped with a thermoelectrically cooled (−70 °C) charge-coupled device (CCD) detector. SERS signals from the samples in capillary tubes were collected using a ×10 objective lens (NA 0.25). The 660 nm laser line from a diode-pumped solid-state laser (Cobolt Flamenco, Sweden) was used as the excitation source. For single-particle SERS measurements, the samples were dropped on a patterned silicon wafer, and SERS spectra were collected by point-by-point mapping with a 1 μm step size. The mapping experiments were performed using a ×100 objective lens (NA 0.90). After the SERS measurement, SEM images of the same area were obtained for single-particle-based analysis.

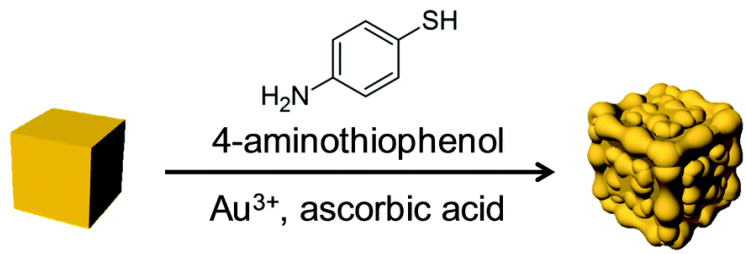

Figure 2.1 A schematic of growth procedure for Au bumpy nanocubes.

Cetyltrimethylammonium bromide (CTAB) and gold (iii) chloride trihydrate ($HAuCl_4 \cdot 3H_2O$) were mixed in the growth solution to create the $AuBr_4^-$ complex. Then, by adding L-ascorbic acid (AA), the complex was reduced to Au^+.[66] In this process, the concentrations of the gold precursor (Au^{3+}) and the reducing agent (AA) were varied to control the degree of growth (Table 2.1). Au NCs as seeds were then added to each growth solution, followed by the addition of 4-ATP. The molar ratio of 4-ATP to Au^{3+} in the growth solution was varied in the range of 1 : 10 to 1 : 200. After aging for 2 h to allow regrowth, the excess chemicals were removed by centrifugation to obtain particle solutions, which exhibited different colors depending on the conditions, as shown in figure 2.2a. The synthesized Au BNCs exhibited stronger, red-shifted, and wider adsorption bands than the Au NCs used as seeds (Au NC_{44}), and these differences became greater with an increase of the concentration of the gold precursor in the growth solution (Figure 2.2b). The number concentration of nanoparticles was maintained (3.0×10^{10} particles per mL) in each sample, and only the size of the nanoparticles changed during the regrowth process.

	CTAB	$HAuCl_4 \cdot 3H_2O$	Ascorbic Acid	4-ATP	Au Nanocubes	ATP : Au^{3+}
	4.7 mL	*0.1 mL*	*0.475 mL*	*0.5 µL*	*50 µL*	
(i)		0.5 mM	5 mM			1 : 10
(ii)		1 mM	10 mM			1 : 20
(iii)		2 mM	20 mM			1 : 40
	1.7 mM			10 mM	3×10^{10} /mL	
(iv)		4 mM	40 mM			1 : 80
(v)		6 mM	60 mM			1 : 120
(vi)		10 mM	100 mM			1 : 200

Table 2.1 Growth conditions for samples Au bumpy nanocubes (i)–(vi)

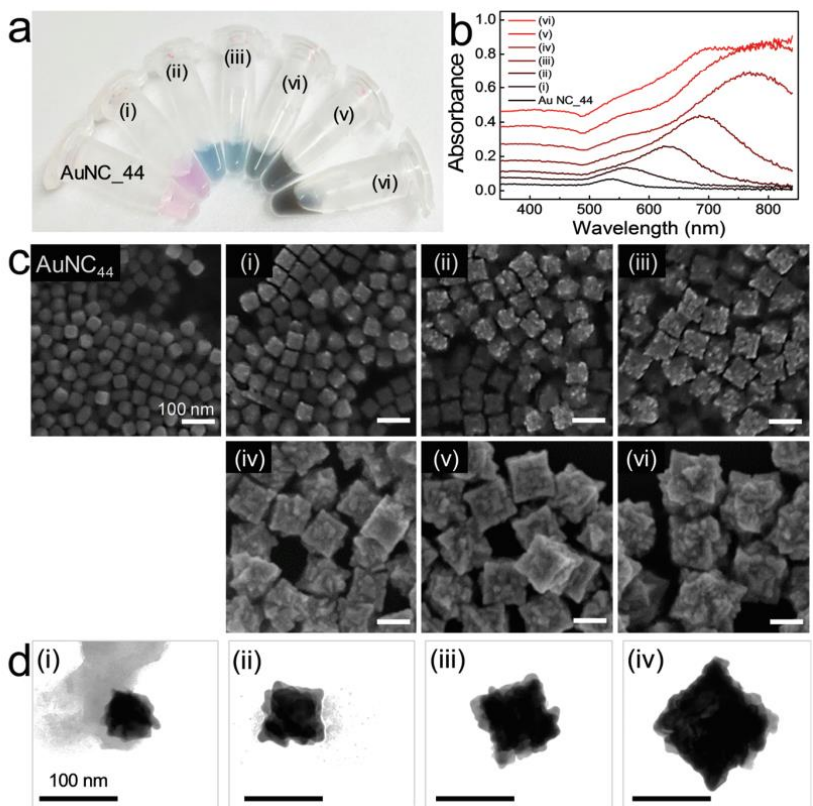

Figure 2.2 Characterization of Au bumpy nanocubes (Au BNCs). (a) Photographs of the solutions of Au nanocubes used as seeds ($AuNC_{44}$) and Au BNCs (i)–(vi) with various growth conditions (b) Extinction spectra of Au BNCs with the same particle concentrations. As the concentration of the growth solution, which includes 4-aminothiophenol, increases, the absorption band of the Au BNCs is red-shifted and the absorption intensity increases. (c) SEM images of the Au BNCs from (a). Increasing the concentration of the growth solution results in larger Au BNCs. (d) TEM images of the Au BNCs obtained with lower concentrations of growth solution ((i)–(iv)).

Figure 2.2c exhibits representative scanning electron microscope (SEM) images of samples (i)–(vi), which have molar ratios of 4-ATP to Au^{3+} of $1:10$, $1:20$, $1:40$, $1:80$, $1:120$, and $1:200$, respectively. In the SEM images, the particles exhibited sizes of 53, 67, 76, 112, 127, and 156 nm with increasing concentration of gold precursor, as expected (Table 2.2). The size distributions of the particles obtained by Nanoparticle Tracking Analysis (NTA) were also shown in figure 2.3. Since the NTA method measures the hydrodynamic size of the particle in solution, the obtained size from the NTA method is slightly larger than that from SEM images. Interestingly, although the size changed dramatically from tens to hundreds of nanometers, the synthesized particles maintained a cubic outline with edges and corners until the molar ratio of 4-ATP to Au^{3+} was $1:120$ (figure 2.2). In addition, the six surfaces of all the particles exhibited numerous small bumps with widths of only a few nanometers in size. In general, it is known that surfaces with bumps and high roughness are able to induce a stronger electromagnetic field enhancement than smooth surfaces. [50] Therefore, we expected that the bumpy surfaces of the newly synthesized cubes would play a significant role in enhancing the SERS signal.

	Mean (nm)
Cube (seed)	*44 ± 4*
(i)	53 *± 4*
(ii)	67 *± 5*
(iii)	76 *± 5*
(iv)	112 *± 6*
(v)	127 *± 8*
(vi)	156 *± 9*

Table 2.2 Size distributions of samples Au bumpy nanocubes (i)–(vi)

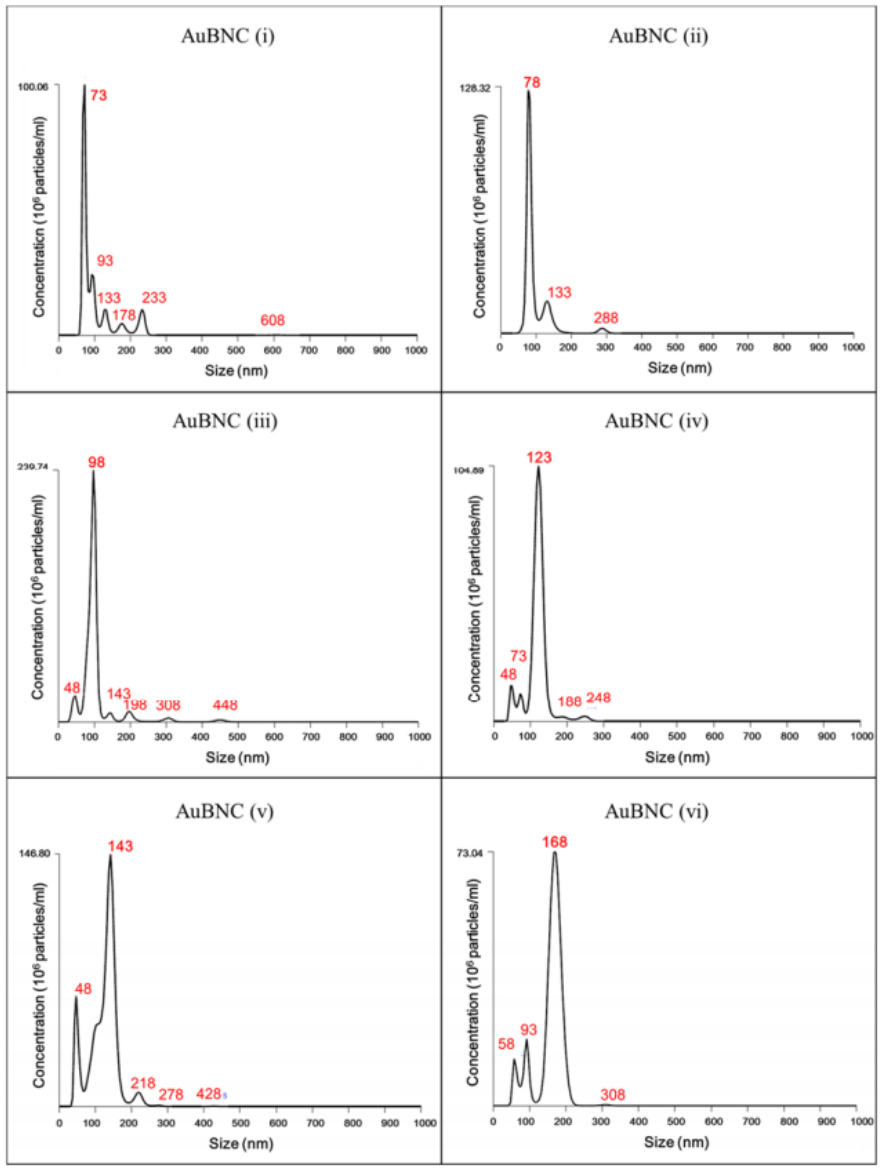

Figure 2.3 Particle size distributions of Au BNCs obtained by Nanoparticle Tracking Analysis.

2.3 Factors affecting Au bumpy nanocube morphology

To understand what factors have a major influence on the bumpy morphology of Au BNCs, the particle synthesis process was performed in the absence of 4-ATP while keeping the other conditions identical. The regrowth process on the NCs without 4-ATP formed nanocrystals with trisoctahedron (TOH) morphologies (figure 2.4b). The TOH shape consists of eight trigonal pyramids, which can form when the eight corners of NCs are pulled out and the resulting faces are sharpened.[67] The average size of these particles with TOH shape was observed as 140 nm. This value is much larger than the size of Au BNC, about 67 nm. We assumed that the gold ions grow from small seed cubes and the organothiol molecules, which have a strong affinity to gold surfaces, were in a competitive situation in the growth process. Then, as the result of this competitive reaction, it was thought that the size of the resultant bumpy particles became smaller in the presence of 4-ATP. The surfaces of the synthesized TOH particles were not corrugated but smooth, implying that the integration of 4-ATP molecules on the gold surface was responsible for inducing the bumpy structure of the Au BNCs

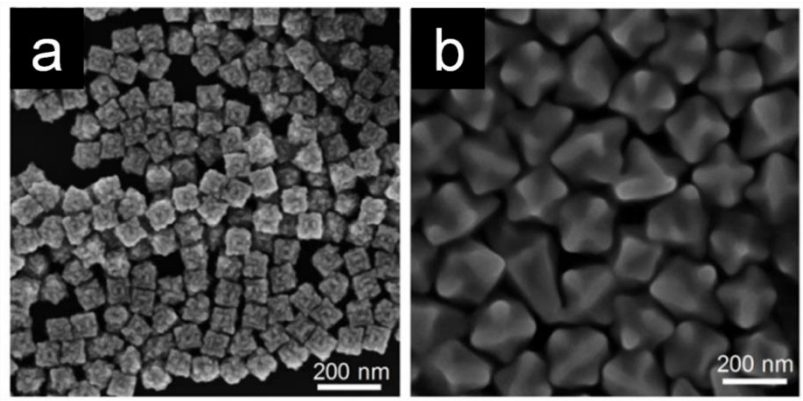

Figure 2.4 SEM images of (a) Au BNCs with average size of 67 nm (iii) at low magnification and (b) trisoctahedron (TOH) nanocrystals with average size of 140 nm obtained by growth of nanocubes under the same conditions as (iii) without 4-ATP.

The thiolate–gold (RS–Au) bond is reported to be as strong as the gold–gold bond, and thiolate-self assembled monolayers (SAMs) on gold surfaces can be usually formed on Au(100) or Au(111).[68] Therefore, we can expect that the thiolate–gold bond significantly modifies the gold–gold bonding at the gold–sulfur interfaces. In the growth solution, 4-ATP molecules containing thiolate compete with Au atoms (generated by reducing Au^{3+}) to attach on the surfaces of Au NCs. In the formation of Au BNCs, it is supposed that selective gold–sulfur bond formation occurred and site selective growth happened. The presence of 4-ATP over the surface of Au BNCs was confirmed by energy-dispersive X-ray spectroscopy (EDX) in figure 2.5. In brief, 4-ATP worked as a site-selective suppressor of the growth process of the gold nanoparticles.

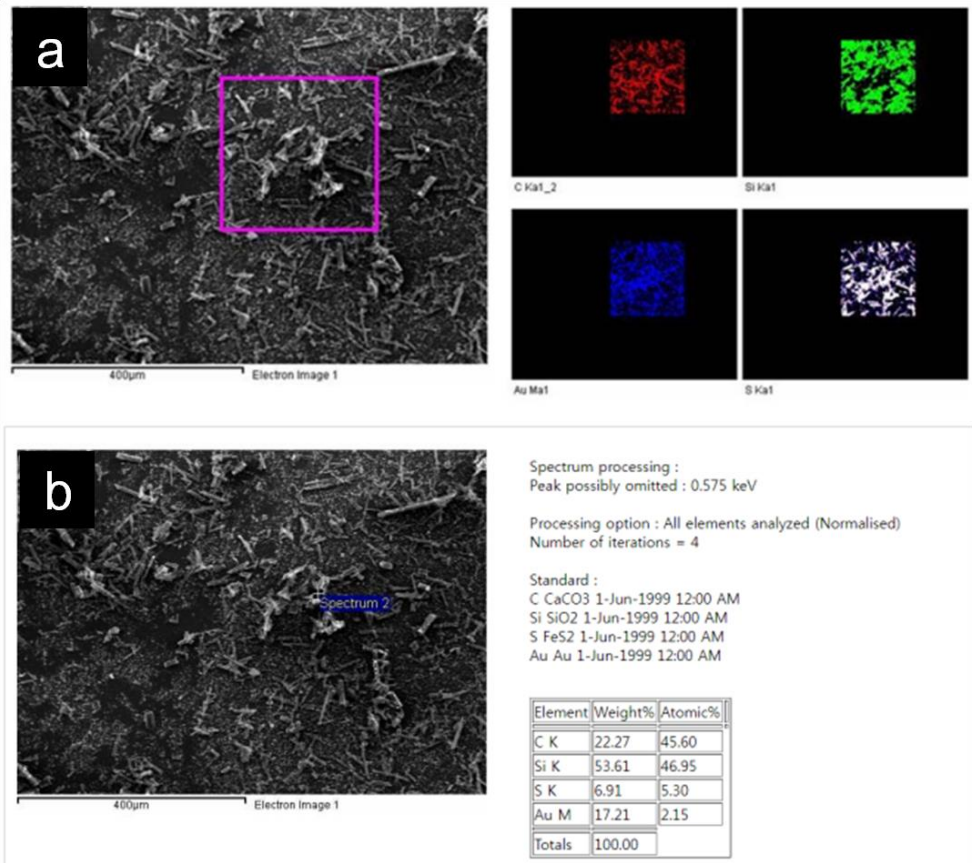

Figure 2.5 Energy-dispersive X-ray spectroscopy analysis of Au bumpy nanocubes. (a) SEM image of Au BNC aggregates on the Silicon wafer and EDX mapping image. Red, green, blue and white colors mean C, Si, Au, and S elements respectively. Au and S appeared at the same location on the SEM image. (b) Quantitative EDX analysis on Au BNC aggregates.

To understand the kinetic effects during the growth of Au BNCs, we varied the sequence in which the reagents were added to the growth solution (figure 2.6). In the basic synthesis process for Au BNCs, the reagents were added in the order of gold precursor, reducing agent (AA), cube seed solution, and 4-ATP, as shown in figure 2.6a. In this case, the obtained particles maintained a cubic shape but exhibited bumpy surfaces and high uniformity. Interestingly, when the sequence of 4-ATP addition was changed, different structures were obtained, as shown in figure 2.6b and 2.6c. Although the surfaces of the particles synthesized in these cases were also bumpy and corrugated, as in the Au BNC case, the uniformity of the particle morphology decreased and the cubic outline disappeared. When the seed cubes were allowed to grow for 5 min before adding 4-ATP (fugure 2.6b), TOH-like nanoparticles with small bumps were generated. Thus, the transformation from cubic to TOH shaped particles occurred in the early stages before the addition of 4-ATP.

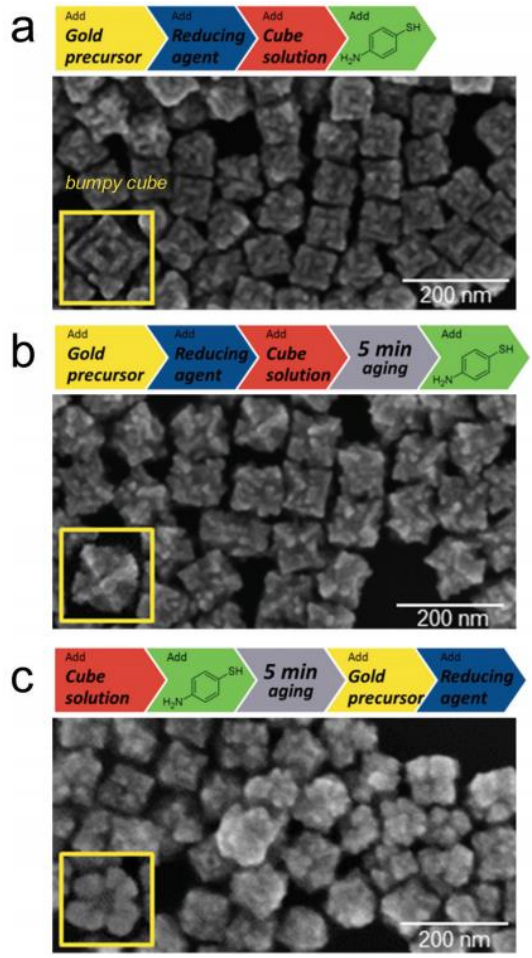

Figure 2.6 Effect of the addition sequence of reagents on the synthetic results. (a) The addition of (1) reducing agent, (2) cube solution (seeds), and (3) 4-ATP solution into the gold precursor (Au^{3+}) solution without aging results in Au BNCs. (b) Trisoctahedron (TOH) morphologies with bumps are obtained when an aging time of 5 min is added between (2) and (3) of (a). (c) Aging the cube solution with 4-ATP before the addition of the gold precursor and reducing agent results in the growth of particles with random and bumpy shapes.

In contrast, when 4-ATP was added to the growth solution and incubated for 5 min before the regrowth of seed cubes (figure 2.6c), irregular structures with bumpy surfaces were generated, without the edges or corners of a polyhedral crystal. Thus, while maintaining the cubic feature, the 4-ATP molecules as suppressors of the growth compete with Au atoms during nanoparticle growth at relatively low concentration of 4-ATP, which implies that a balance between growth and its suppression is a key factor for controlling the morphology of Au BNCs. In our previous study, [66] overgrowth conditions for rhombic dodecahedrons with a modifier (4-ATP) led to the formation of concave structures, whereas less favorable growth conditions (lower concentrations of Au^{3+}) of NC resulted in the cubic outline being maintained. Although bumpy TOH-like nanoparticles also have feasibility as SERS substrates, Au BNCs were taken to have more advantages in terms of the homogeneity and further application such as generation of 2D square arrays. [69]

When the temperature increased, the particles typically formed more random and rounded shapes by our seed mediated method using organothiol. This can be due to the decreased selective growth (more random facet growing) by the faster reduction and diffusion of the gold atoms as the temperature increases.[70]

2.4 SERS characterization of Au bumpy nanocubes

To further characterize the Au BNCs, SERS spectra of solutions of Au BNCs (i)–(vi) were obtained using 660 nm laser excitation (figure 2.7). The typical SERS spectra of 4-ATP was obtained with Au BNCs (i)–(vi), demonstrating that 4-ATP molecules, as shape modifiers, were successfully immobilized on the Au surfaces, where they acted as a Raman labeling compound. Au BNCs (i)–(vi) all showed greater SERS intensities than Au NC_{44}, but the maximum intensity was observed for Au BNC (iii), which had a size of *ca.* 76 nm (Au BNC_{76}). This result seems to be counterintuitive because the far-field scattering intensity at the excitation wavelength (660 nm) increased as the nanoparticle size became larger, although the maxima of the absorption band shifted to longer wavelengths with increasing particle size, as shown in figure 2.2b.

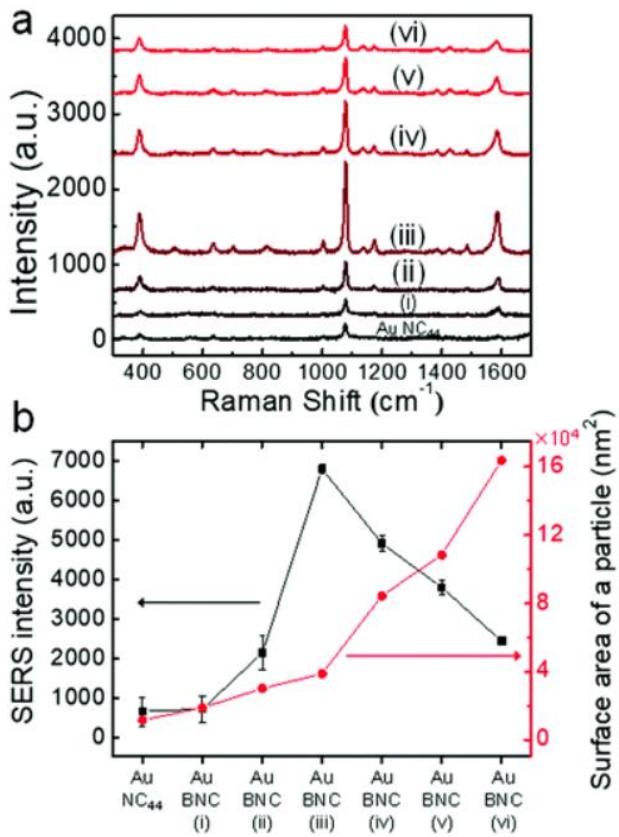

Figure 2.7 SERS analysis of Au bumpy nanocube solutions (i)–(vi). (a) Raman spectra of the Au BNCs obtained with photoexcitation at 660 nm, a sample power of 30 mW, and an acquisition time of 1 s. (b) SERS intensities from Au BNC solutions (i)–(vi) using the 385 cm^{-1} band and the surface area of a particle.

The analysis of SERS intensities for Au BNCs was approached in terms of two factors. The first one is the number of Raman label compound molecules on the surface due to the different size and shape of nanoparticles, and the second one is the signal enhancing ability that mainly relates to the nanostructures of substrate under the given photoexcitation wavelength. According to the calculations, the observed SERS intensities and estimated surface areas for the different Au BNCs were plotted in figure 2.7. The SERS intensities increase from seed to Au BNC (iii) and then decrease to Au BNC (vi) while the surface area of the particles increase gradually as the particle size increases. This result indicates that Au BNC (iii) as SERS substrate has the strongest enhancing ability.

Considering the surface plasmon resonance (SPR), shown as the extinctions of Au BNCs (i)–(vi) in figure 2.2b, one could expect that when Au BNCs grow larger, average electromagnetic field enhancement under 660 nm photo-excitation would increase through SPR. However, in our experiment, the optimal point of the SERS enhancement was observed in Au BNC (iii) (Au BNC_{76}). This can be interpreted by the interaction between bumpy structures on the cubic body in reference to previous studies.[71] It is well known that the near-field is much more strongly affected by the local morphology of a nanoparticle than the far-field response in all tightly confined plasmonic cavities.[72] The effective sites for SERS in our Au BNCs are considered as the gaps between the small bumpy structures, and the curvature of small particles contributes the

extent of SERS activity. Considering the local structure of Au BNCs shown in the TEM images of figure 2.2d, a simple model is proposed that the size and number of small bumpy particles increase as Au BNCs grow from a cubic seed in their synthetic processes, as shown in the schematic illustration in figure 2.8. In the early case of Au BNC (*e.g.* Au BNC (i)), the bumpy structures are less developed and their numbers are low, illustrating that their SERS effect is not significant. In the case of Au BNC (iii), the bumpy structures have grown and developed many interstitial gaps between the bumpy particles, illustrating that this structure is more effective in terms of the SERS effect than the earlier ones. However, as the Au BNCs grow further, as in the case of Au BNC (v), merging the bumpy structures flattens and smoothens the gap structure, which produces a less effective SERS effect. Therefore, it is thought that the surface roughness [46] of Au BNCs increases to Au BNC (iii) and then decreases, and the optimal point of the surface roughness, which maximizes the local electromagnetic fields for SERS, is at Au BNC (iii) on the basis of the experimental data of figure 2.7b.

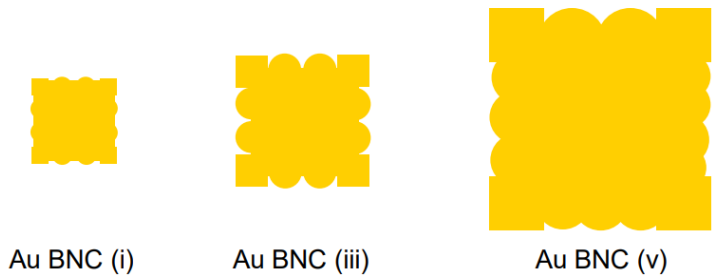

Figure 2.8 Schematic illustrations for development of surface morphology as Au BNCs grow larger. In the early case of Au BNC (e.g. Au BNC (i)), bumpy structures are less developed and their numbers are low, illustrating that their SERS effect is not significant. In the case of Au BNC (iii), bumpy structures are much grown to have many interstitial gaps between bumpy particles, illustrating that this structure is more effective in SERS effect than the earlier ones. However, as the Au BNCs grow further as in the case of Au BNC (v), merging the bumpy structures flattens and smoothens the gap structure, which becomes less effective in SERS effect.

To validate the potential of the Au BNCs as SERS nanoprobes, a comparative SERS analysis was performed. As shown in figure 2.10a, we also prepared Au NCs with an edge length of *ca.* 75 nm (Au NC_{75}) for comparison with Au BNC_{76}. The extinction spectra of Au NC_{44} (used as seeds), Au NC_{75}, and Au BNC_{76} are shown in figure 2.9. Before the Raman measurement, Au NC_{44}, Au NC_{75}, and Au BNC_{76} were incubated with the same concentration of 4-ATP to ensure that 4-ATP covered the available surfaces of the nanoparticles. Although the as-prepared Au BNC_{76} have a sufficient SERS signal to measure without additional 4-ATP treatment, we wanted to have the surfaces of Au $BNCs_{76}$ completely saturated with 4-ATP, as in Au NC_{44} and An NC_{75}. The result showed that the signal intensity of Au $BNCs_{76}$ was increased 2.6-fold compared to the signal before additional treatment of 4-ATP (figure 2.7), which implies the surfaces of the Au BNCs were partially exposed and therefore still available for further modification in the as-prepared state. As shown in figure 2.10, the SERS intensity obtained from Au BNC_{76} is obviously much stronger than those obtained from the other two Au NCs. The Au BNCs exhibited an 18-fold stronger SERS intensity than the 44 nm Au NCs and a 15-fold stronger SERS intensity than the 75 nm Au NCs. According to the simple modeling, it was estimated that Au BNC_{76} have a total 3.3-fold surface area contribution compared to Au NC_{22}. Furthermore, the effect of surface area between Au NC_{75} and Au BNC_{76} mostly comes from the difference in their morphology, which is responsible for an about 1.2-fold contribution to the increased signal.

Therefore, the signal increase of more than 10-fold is regarded to originate from hot spots generated by bumpy structures.

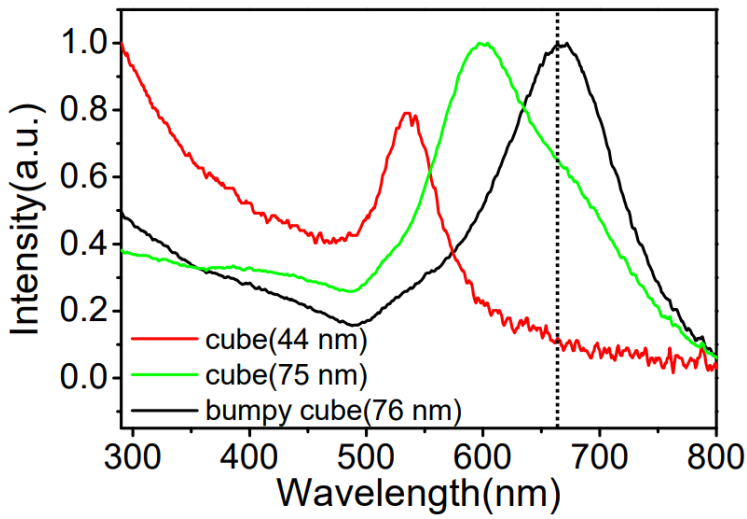

Figure 2.9 Extinction spectra of Au nanocubes (44 nm), Au nanocubes (75 nm), and Au bumpy nanocubes (76 nm).

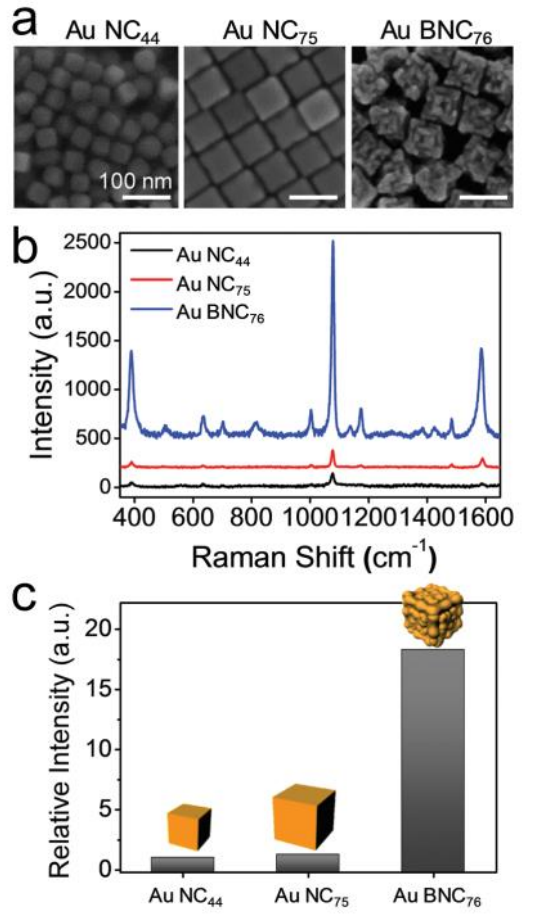

Figure 2.10 Comparative SERS analysis (a) SEM images of Au NCs_{44}, Au NCs_{75}, and Au $BNCs_{76}$. The subscripts denote the mean edge length of the particle. (b) SERS spectra after conjugation of 4-aminothiophenol under the same conditions. (c) SERS intensities of Au NCs_{44}, Au NCs_{75}, and Au $BNCs_{76}$ from (b) normalized to the intensity of Au NC_{44}. The Au $BNCs_{76}$ produced a 18.3-fold higher signal than Au NCs_{44} and a 14.6-fold higher signal than Au NCs_{75}.

2.5 Single-particle SERS measurements and polarization dependence

We then performed SERS measurements on single Au BNC particles. First, we prepared Au BNC_{76}-loaded substrates for SERS intensity mapping by drop-casting onto a silicon wafer. Then, the Raman signal was collected using point-by-point measurements. The step size of the mapping measurement was 1 μm and the acquisition time was 3 s with 660 nm photoexcitation (0.14 mW). The area scanned for Raman was identical to that in the SEM image to allow correlation of the SERS intensity and the surface morphology of each Au BNC_{76} particle. Figure 2.11a shows a representative SERS spectrum obtained from a single Au BNC_{76} particle. Most of the Raman bands are characteristic SERS bands of 4-ATP, and some weak SERS bands at 1140, 1188, 1386, and 1432 cm^{-1} which originate from 4-4′-dimercaptoazobenzene (DMAB) were observed.[73] Even though DMAB can be produced at the hotspot of the SERS substrate where the field enhancement is very high, the relatively weak intensity of intensity of these Raman band implies that a high turnover rate did not occur on the Au BNC surfaces. Overlaying the Raman intensity map on the SEM image shows that areas of high SERS intensity correspond to the positions of single particles (figure 2.11b). The SERS enhancement factors (EFs) of the Au BNC particles were estimated by considering the 1085 cm^{-1} band assigned to the

C–S stretching vibration.[74] For 40 Au BNC_{76} particles, the average value of the SERS EFs was found to be 7×10^5 with a small deviation (figure 2.11c).

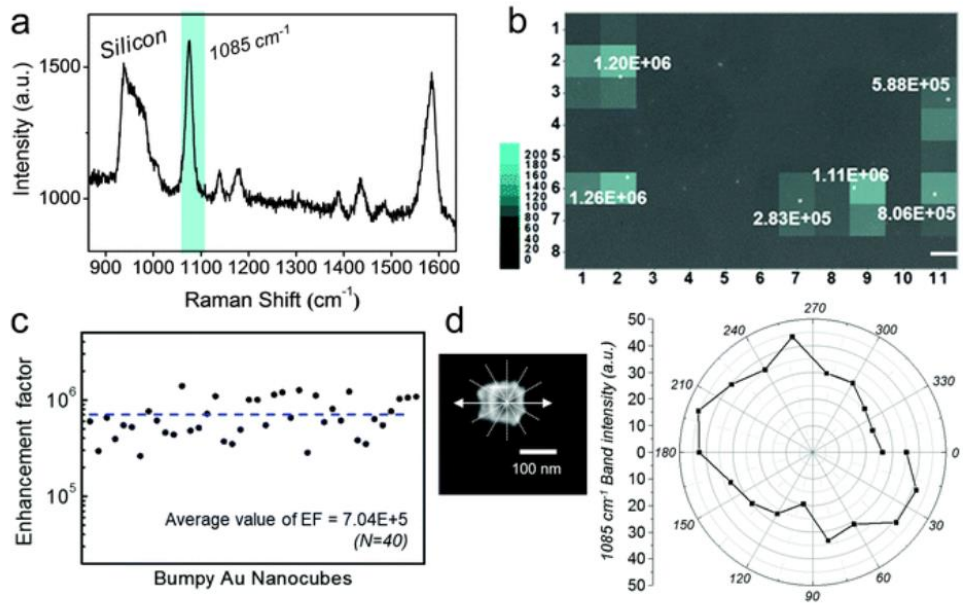

Figure 2.11 Single particle detection of Au BNCs. (a) Typical SERS spectrum obtained from a single Au BNC_{76} particle on a silicon wafer. (b) SERS intensity map with enhancement factor (EF) values at the 1085 cm^{-1} band of 4-ATP. The intensity map is overlaid with the corresponding SEM image. The scale bar is 1 μm. (c) EF distribution for Au BNCs (N = 40). The average EF value was 7×10^5. (d) Polar plot of the SERS intensities for the 1085 cm^{-1} band with an SEM image of the corresponding single Au BNC_{76} particle.

Considering the cubic structure of the Au BNCs, to explore if there is any angular dependence on incident light polarization, a polarization-dependent SERS measurement was performed on a single Au BNC_{76} particle. Using 660 nm laser radiation, we obtained a series of SERS spectra by rotating the polarization in 20° steps (figure 2.12). In the case of NCs, dramatic variations in SERS intensity have been reported when the polarization of the excitation laser is oriented at different angles relative to the cubes, and the signals are generally more strongly enhanced when the laser is polarized along a face diagonal. [64] Interestingly, this strong angular dependence vanished when the NCs had many bumps, as shown in figure 2.11d. We interpreted this strong SERS intensity to be due to the bumpy hot spots generated all over the nanoparticle and the homogenous distribution of these hot spots. The bumpy surface of this cube-like particle with high SERS sensitivity and an omnidirectional radiation pattern is highly desirable for reliable detection and diagnosis applications.

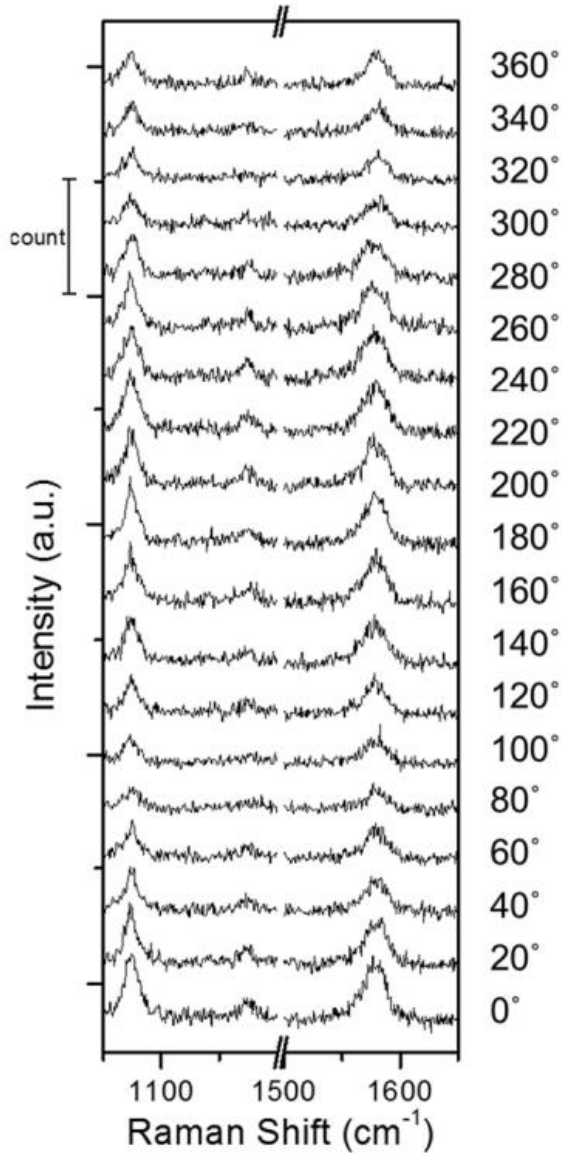

Figure 2.12 Polarization-dependent SERS spectra from the single Au BNC shown in figure 2.11d.

2.6 Conclusion

We synthesized Au bumpy nanocubes(AuBNCs) with strong SERS intensity by controlling the regrowth of Au NCs. Using 4-ATP as an additive during the growth stage, Au BNCs of various sizes were produced while maintaining the cubic outline. Au BNCs exhibited much stronger SERS signals than Au NCs, with the highest SERS signal obtained from Au BNC with a size of 76 nm. In addition, the Raman signal attained single-particle detection under the visible range. In future, this new particle is expected to be applied as an ultrasensitive SERS nanoprobe and nanoantenna in a variety of fields owing to its cubic outline, high uniformity, and ease of adjusting the particle size by controlling the precursor concentration.

Chapter 3. Tuning optical property of chiral gold nanoparticles by introducing oligonucleotides

3.1 Introduction

Chirality, a structural property prevalent in nature, refers to a geometrical orientation being non-superimposable to each other. Especially in the field of plasmonics, strong chiral light-matter interaction has been one of the fundamental needs with its wide potential application in chiral recognition sensing, optical metamaterials, enantioselective catalysis, and opto-tele communication technologies.[37,75-79] In this sense, relentless efforts have been dedicated to construction of chiral plasmonic nanostructures using E - beam lithography,[80-82] direct laser writing,[83] and macromolecular assembly.[84-86] Despite sophisticated control of chiral nanostructures, current state of art technologies require complicated synthetic processes and possess limitations on constructible morphologies. Therefore, facile synthesis methods to precisely control chirality in nanoscale still remains as a scientific and engineering challenge. Recently, synthesis of a three-dimensional chiral gold nanoparticle has been achieved through a novel aqueous based chemical seed-mediated method.[87] Amino-acid and peptide induced synthesis of chiral gold nanoparticle utilize incorporation of thiol containing bio-molecular additives such as cysteine or glutathione molecules into a well-known seed mediated method. Seed

mediated method has been well known for its precise morphology control, ranging from thermodynamically stable lowindex facets to more complex, thermodynamically unstable highMiller-index surfaces.[67,88] The chiral kink sites in high-indexed nanoparticles are composed of atomic arrangement with R and S orientation in equal ratio, forming an achiral symmetric structure. (figure 3.1) Upon introduction of chiral molecules during the growth process, enantioselective interaction between chiral molecules and intrinsically chiral kink sites of nanoparticles promote an asymmetric growth with unequal ratio of R and S plane generation, forming the overall chiral nanostructures. With dissymmetry of the R and S regions, the original $4/m\,\bar{3}\,2/m$ point group symmetry of the seed nanoparticles was changed to 432 point-group symmetry. Therefore, synthesized single plasmonic chiral gold nanoparticles were named as 432 helicoid series after its unique 432 point-group symmetry and the representative helicoidal morphology.

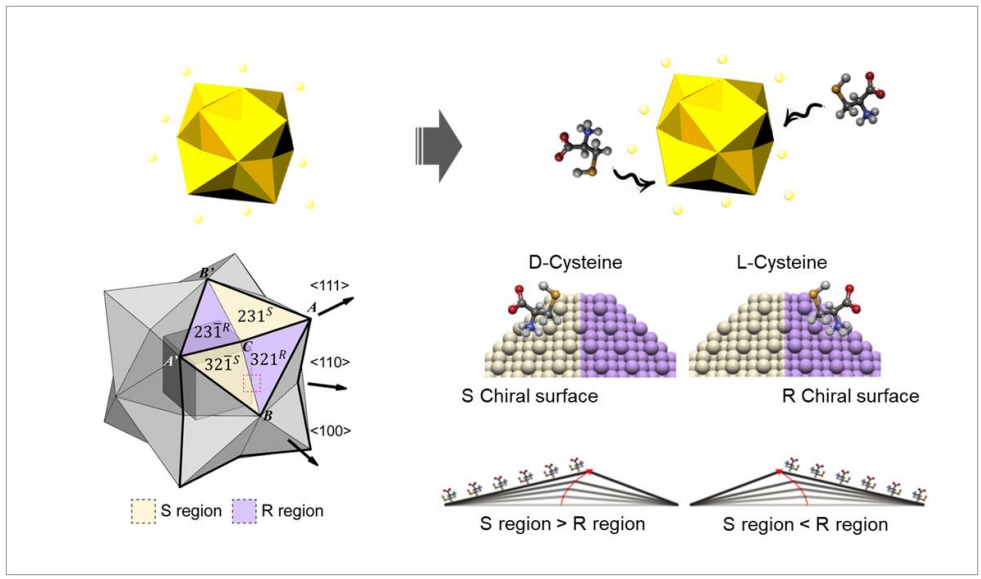

Figure 3.1 Mechanism of chirality evolution through the interplay between the enantioselective binding of molecules and the asymmetric growth of high-index facets.

The most significant advantage of amino-acid and peptide induced chiral gold nanoparticle synthesis is its versatile and precise control of chiral nano-morphologies in 100 nm scale with flexible tuning of chiroptic responses. While retaining the starting seed morphology to 100 enclosed nanocube, change of chirality inducing bio-molecules, cysteine and glutathione, strongly influence the chiral morphology development, resulting in completely different morphology and chiroptic response. Aside from small bio-molecular additives for nanoparticle morphology control,[66,89,90] larger size scale of bio-molecular additives such as oligonucleotide has recently been utilized for nanoparticle morphology control in seed-mediated method.[91-93] In this regard, our group proposed the dynamic control of chirality evolution in metal nanoparticles synthesis using wide ranges of multi-scale biological encoders.[94] This versatile control of chirality could provide a new synthetic insight into chiral nanomaterials and provide foundation for dynamic imbuement of chirality to extend the range of accessible nano-photonic design. (figure 3.2)

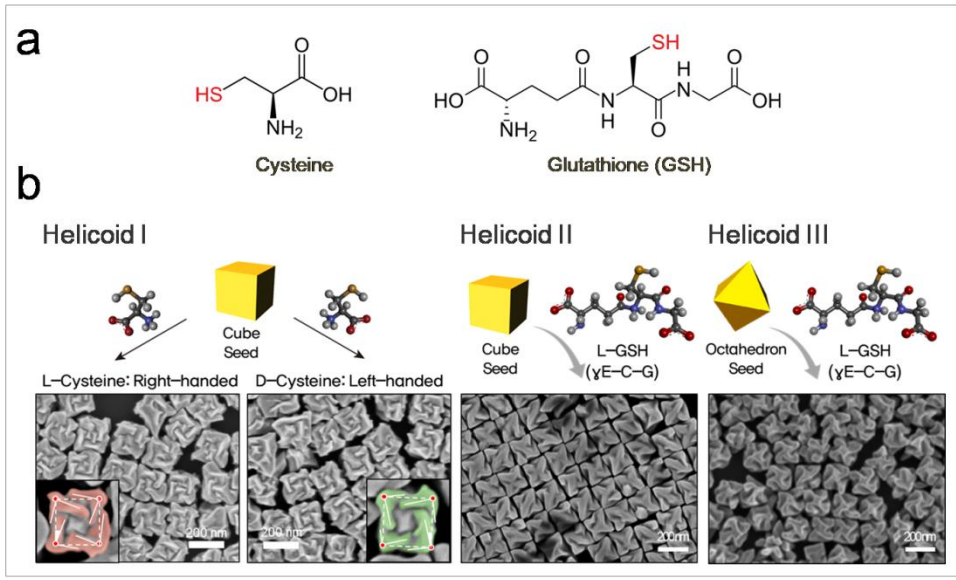

Figure 3.2 (a) Structural formula of thiol-containing chiral organic molecules, cysteine and glutathione (b) The resultant chiral 432 helicoid nanoparticles using different seed morphology and chiral organic molecules.

3.2 Thiolated oligonucleotide conjugation to chiral 432 helicoid nanoparticles

The introduction of biomolecular oligonucleotides into chiral 432 helicoid nanoparticles has been studied to control their optical properties. In order to make the nucleic acid molecules adhere well to the gold nanosurface, a strategy of adding thiol having high affinity to gold at the end of the oligonucleotide is widely used.[95,96] Oligonucleotides, thymine 20 mer with thiol modification, were purchased from Integrated DNA Technologies. Figure 3.3 shows a brief schematic of the experimental procedure for conjugating thiolated oligonucleotides to 432 helicoid III nanoparticles. Here thiolated oligonucleotide molecules should be used after treatment with tris (2-carboxyethyl) phosphine (TCEP). Thiolated oligonucleotide molecules are not supplied as free thiols. Generally, the 5 and 3 terminal thiol ends are blocked by disulfde bonds. TCEP molecules can be used to cleave the disulfide bonds and produce free thiol on oligonucleotide. Purification process is needed, because without purification, the cleaved fragment is still in the solution and can also adsorb on the gold nanoparticle surfaces.[95]

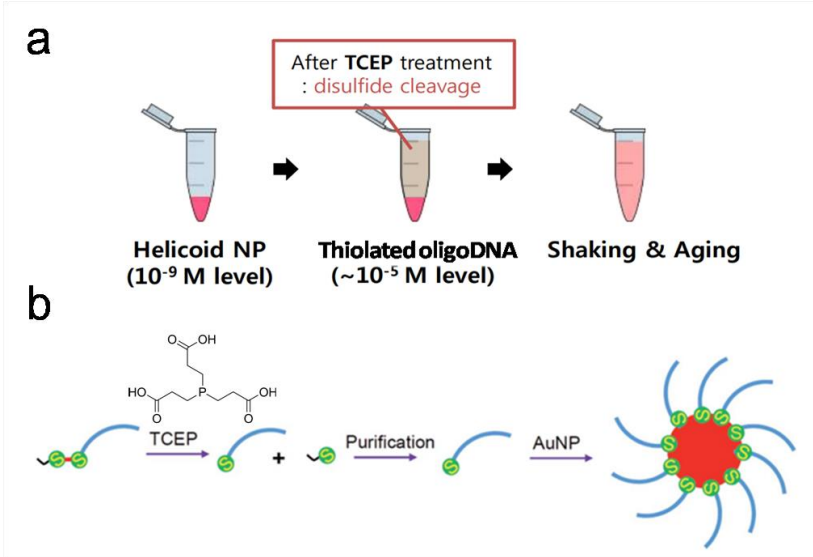

Figure 3.3 (a) A schematic of the experimental procedure for conjugating thiolated oligonucleotides to gold nanoparticles. (b) Thiolated oligonucleotide molecules should be used after treatment with tris (2-carboxyethyl) phosphine (TCEP) and purification.

The salt stability of oligonucleotide-conjugated 432 helicoid nanoparticles was confirmed by measurement of UV– vis extinction spectra (figure 3.4). Oligonucleotide-conjugated helicoids nanoparticles were stable up to 14 mM $MgCl_2$ (figure 3.4). At higher $MgCl_2$ concentrations, nanoparticles were aggregated and particle solutions became transparent.

Raman scattering spectra measurements also confirmed that oligonucleotides were conjugated to the gold nanoparticle surface. Figure 3.5 shows Raman scattering spectra measured after reacting 432 helicoid III nanoparticles in the oligonucleotide solution with concentrations of 0 M and 10 μM. In case of T20 10 μM concentration, the peak of 1080 Raman shift, PO_2^- symmetric stretching, originated from oligonucleotide backbone structure was observed with strong intensity. This could be evidence of oligonucleotide conjugation on the surface of gold nanoparticles.

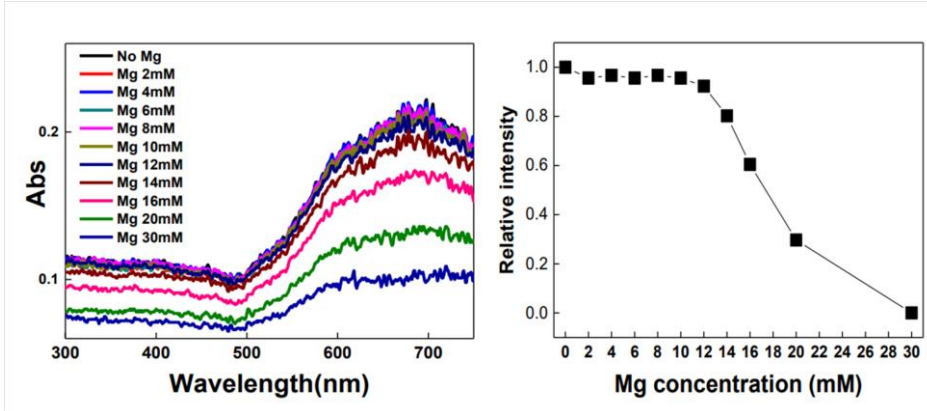

Figure 3.4 Salt stability test of oligonucleotide-conjugated 432 helicoid nanoparticles by measurement of UV– vis extinction spectra

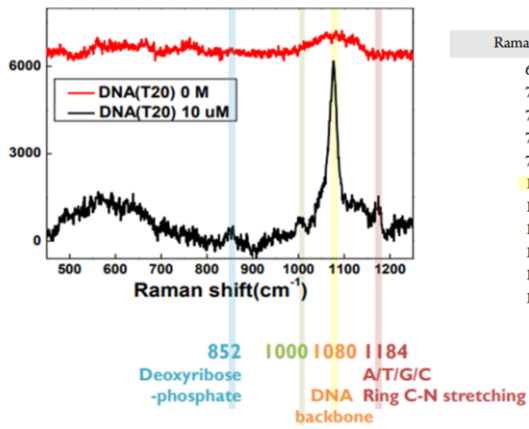

Raman bands (cm^{-1})	assignments
675	G, ring breathing
723	A, ring breathing
739	T, ring breathing
776[b]	C, ring breathing
786	PO_2^-, skeleton stretching
1087	PO_2^-, symmetric stretching
1240/1248	A, C, or T, ring stretching
1327	A
1436	CH_2, deformation
1570	A, G
1631/1643	T, C

Figure 3.5 Raman spectra measured after reacting 432 helicoid III nanoparticles in the oligonucleotide solution with concentrations of 0 M and 10 μM

3.3 Chiral 432 helicoid II nanoparticle synthesized with glutathione and poly(T)20 nucleotide

We demonstrate two-fold increase of chiroptic response of 432 helicoid II nanoparticles by additional introduction of homooligonucleotides consisting of thymine poly(T)20 (T20) as a secondary chiral modifier. Chiroptic response of newly synthesized 432 helicoid II shows dependency to the input T20 concentration which specific ratio of T20 concentration induce the most significant chirality enhancement. Time-resolved growth pathway analysis of 432 helicoid II with T20 supports involvement of T20 during the initial generation for high-index facets which induce subsequent chiral gap structures through the selective interaction with glutathione molecules.

Experimental scheme of 432 helicoid II with T20 additives is shown in figure 3.6. For conventional 432 helicoid II nanoparticles, uniformly synthesized gold cubic nanoparticles enclosed with 100 facet are used. In the case of no glutathione molecule added during the synthesis, symmetric and achiral nanoparticles were synthesized. Upon the addition of chiral glutathione molecules, generated high-index facets and chiral glutathione molecules undergo an enantioselective interaction to break the mirror and inversion symmetry of the resulting nanoparticles. Chiral features of 432 helicoid II gradually progress by generation of high-index facets, which further develops into expanded and

distorted edges of rhombus to generate chiral gap structures. Growth propensity is strongly affected with existing molecules in the growth solution, which allows potential modification of synthesis. In the present synthetic method, a synergistic effect of multiple chiral biomolecules has been demonstrated. During the synthesis, homooligonucleotides consisting of thymine were introduced into the 432 helicoid II growth solution to co-exist as a chiral modifier along with the already present chiral glutathione molecules.

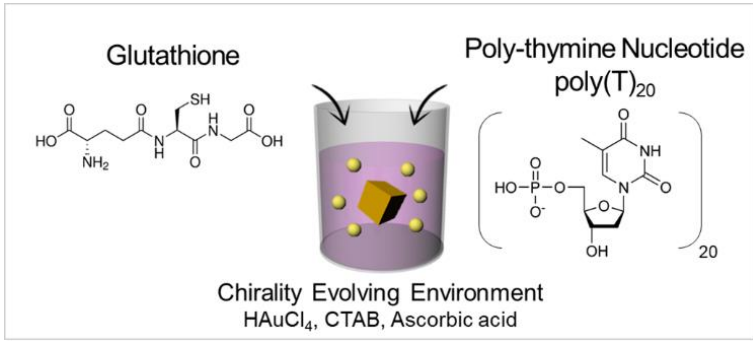

Figure 3.6 Experimental scheme of synthesis for 432 helicoid II with T20 additives. Initial nanocube is added into growth solution containing glutathione molecules and oligonucleotide molecules.

Co-existence of T20 with glutathione molecule induced significant enhancement in the chirality of 432 helicoid II as shown in figure 3.7a and b. The 432 helicoid II synthesized with T20 shows preservation of representative pin-wheel like chiral motif as previously reported. According to previous simulation results, chiroptic response is closely related with the chiral gap structures, where slight change in the chiral gap geometry could induce significant change in the chiroptic response.[87] The newly synthesized 432 helicoid II with T20 shows difference in the chiral gap structures, where changes in depth and tilt of chiral gap structures are observable compared to conventional 432 helicoid II. The effect of T20 on the overall chiral development is more clearly visible in the chiroptic response. In figure 3.7 b, the chiroptic response comparison between conventional 432 helicoid II and 432 helicoid II with T20 is shown. Surprisingly, introduction of T20 to the typical 432 helicoid II synthesis showed dissymmetric value of g = 0.08, which is twofold increase of 432 helicoid II. The dissymmetric factor of g = 0.08 was never achieved under typical condition of 432 helicoid II synthesis using only glutathione molecule with cubic seed nanoparticles regardless of molecular concentration.

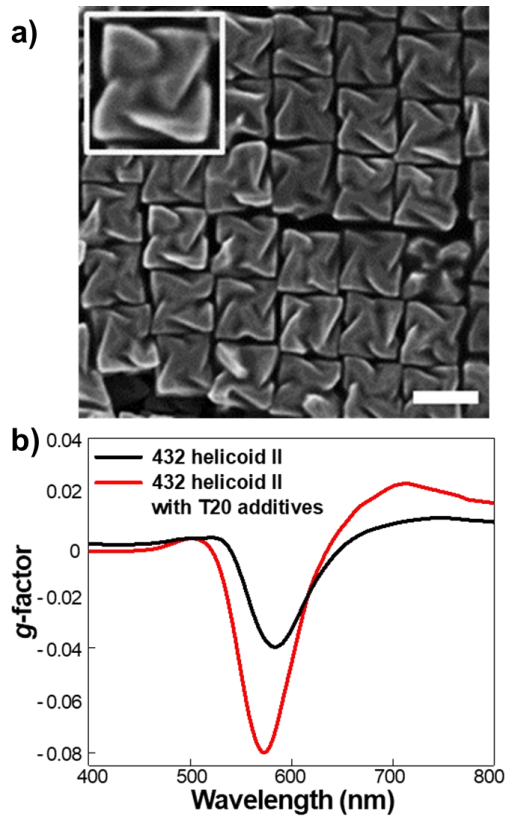

Figure 3.7 Comparison between conventional 432 helicoid II and 432 helicoid II with T20 additives. (a) Low magnification SEM images of newly synthesized 432 helicoid II with T20 additives. Inset shows high-magnification of 432 helicoid II with T20 additives viewed from direction. (b) Chiroptical response of 432 helicoid II and 432 helicoid II with T20 additives. (Scale bars = 200 nm)

Increase in dissymmetric factor of 432 helicoid II with T20 is observed respect to change in T20 concentrations in figure 3.8a and b. While maintaining the glutathione concentration to 2.5 μM, incremental concentrations of T20 has been applied. Addition of T20 results in gradual increase of chiroptic response. Change in chiroptic response respect to input T20 concentration is more clearly definable in figure 3.8b, where the maximum dissymmetric factor has been recorded regardless of the peak positions. When no T20 molecules were introduced to the growth solution, the dissymmetric factor of 432 helicoid II shows the previously reported value of g = 0.04. With the increasing concentrations of T20, dissymmetric factor gradually increase to reach g = 0.08 at T20 concentration of 0.5 μM. The dissymmetric factor remains similar up to 1.0 μM concentration of T20, but further increase of T20 concentrations to 2.5 μM results in deterioration of dissymmetric factor. Gradual increase in dissymmetric factor respect to the increase in input T20 concentrations up to the optimum concentration of 0.5 μM strongly indicate that T20 is involved in the chirality evolution of 432 helicoid II.

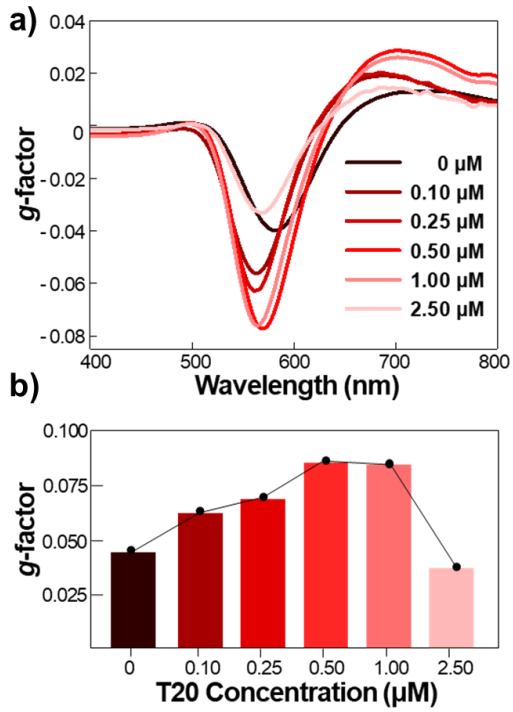

Figure 3.8 Change in dissymetric factor of 432 helicoid II respect to change in T20 concentration. (a) Dissymmetric factor spectrum respect to change in T20 concentration. (b) Bar graph of maximum dissymetric factor regardless of peak position. Solid line shows the trend of dissymetric factor change of 432 helicoid II with T20.

As to more closely understand the contribution of T20 to the chirality evolution of 432 helicoid II, concentration ratio dependent chiroptical response change has been observed while retaining the total bio-molecular additives to 2.5 μM as shown in figure 3.9a. When only T20 was used as an additive, no sign of chiroptic response was observed. The dissymmetric factor of 432 helicoid II with T20 reaches its maximum when molar ratio of T20 and glutathione is 1: 3. The role of T20 molecules during the chirality evolution is more clearly visible when maximum dissymmetric factor is plotted regardless of the peak positions as shown in figure 3.9b. Despite increase of T20 concentrations, synthesized nanoparticles show no chiroptic response. This indicate that T20 molecule is not directly involved in the chirality evolution process and only using T20 could not synthesize chiral nanoparticles. On the other hand, increase of chiroptic response is clearly visible when glutathione concentration was increased. Most significant result is when both biomolecules simultaneously exist in the growth solution. When a specific ratio of T20 was added respect to glutathione concentration, the dissymmetric factor was significantly enhanced. This indicates that while glutathione molecule serves a dominant role during the chirality evolution, T20 molecules also provide a synergistic effect to accelerate the chirality evolution.

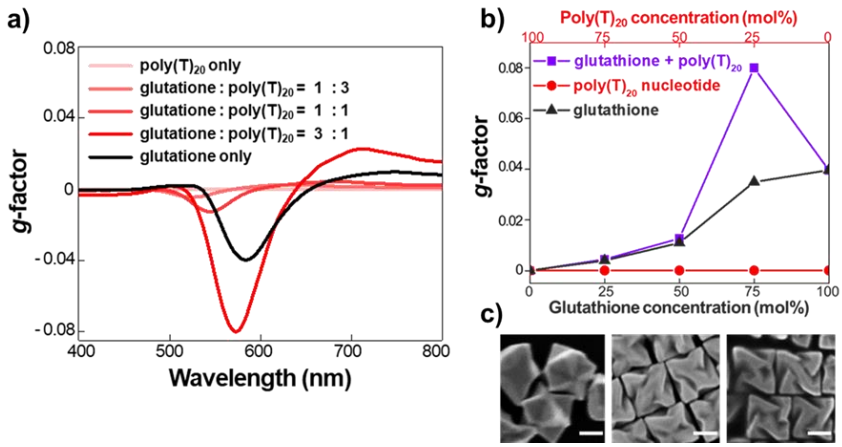

Figure 3.9 Change in chirality evolution respect to the relative ratio of glutathione and T20 concentrations. (a) Dissymmetric factor spectrum of 432 helicoid II and 432 helicoid II with T20 additives. (b) Maximum dissymmetric factor plotted regardless of the peak positions. Violet line : co-existence of glutathione and T20, red line : T20, and black line : glutathione (c) SEM images of synthesized nanoparticles with T20(left), conventional 432 helicoid II (middle), and T20 added 432 helicoid II with highest dissymmetric factor (right).

Morphology of synthesized nanoparticles are shown in figure 3.9c. Nanoparticle synthesized only with T20 (left) shows clear achiral high-index morphology whereas both nanoparticles with glutathione (middle and right images in figure 3.9c) shows chiral development. Compared to cubic seeds grown without any additives introduced to growth solution, nanoparticle synthesized with T20 shows more distinct facet development. According to previous studies using oligonucleotide molecules for morphology control in seed-mediated growth of achiral nanoparticles, oligonucleotide molecules have been described to passivate seed surfaces or to kinetically affect the deposition of metal to induce morphological changes.[92,93]

Therefore, in effort to understand the detailed effect of T20 on the chirality evolution, injection time of T20 has been controlled as shown in figure 4. According to our previous in situ study of 432 helicoid II synthesis, there are two distinct moments of acute chirality evolution kinetic changes, at 40 minutes of the reaction time and 80 minutes of the reaction time. The growth stage between 0 minutes to 40 minutes of reaction time is strongly related with the generation of high-index facets and chiral motifs by the tilting of edges between R-S boundaries. The growth stage between 40 minutes to 80 minutes of reaction time is known to be dedicated to development of cubic outer boundaries and increase in depth of chiral cavity. In the final stage of the growth between 80 minutes to 120 minutes, further stabilization of cubical outer boundaries and 100 facets are dominating.[87] Therefore, based on our previous knowledge on the

growth pathway of 432 helicoid II, introduction of T20 molecules to the glutathione containing growth solution has been performed at distinct moments of chiral growth kinetic changes, 0, 40, and 80 minutes of the reaction. The in situ Circular Dichroism (CD) measurements shown in figure 3.10 are the progressive chiroptic response increase respect to T20 incorporation time. Chiroptic responses show increased CD spectra with a gradual shift in peak positions towards larger wavelength, indicating the increase of nanoparticle size. Among spectra, 432 helicoid II with T20 inserted at 0 minutes of the reaction shows the highest CD response followed by T20 inserted at 40 minutes. The 432 helicoid II with T20 inserted at 80 minutes of the reaction shows no distinguishable change to the conventional 432 helicoid II chiroptic response.

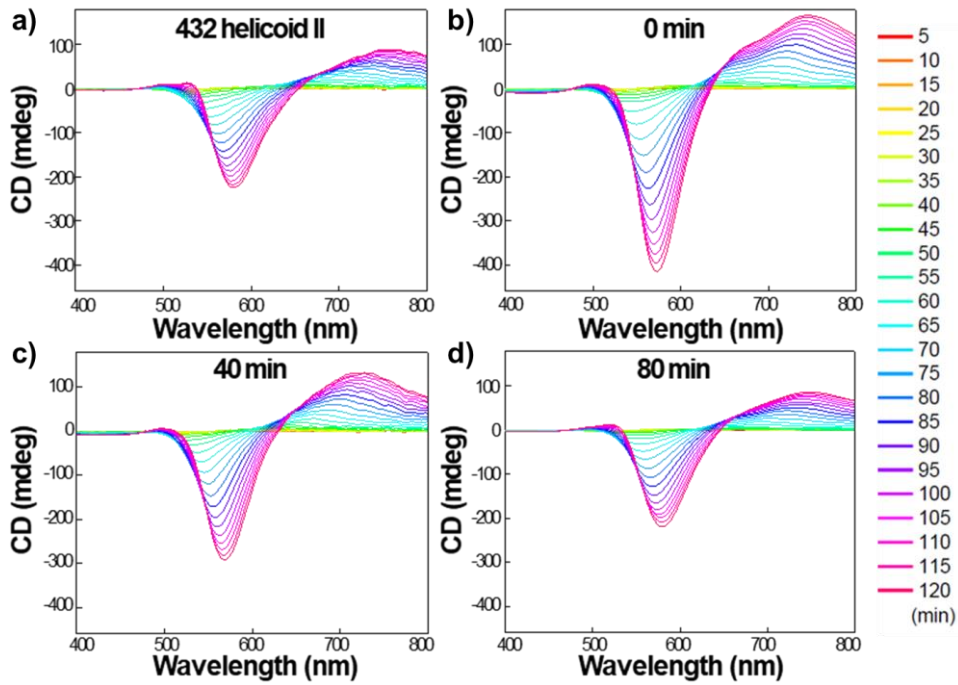

Figure 3.10 Time-resolved CD measurement of 432 helicoid II and newly synthesized 432 helicoid II with T20. CD spectra were measured every 5 minutes. (a) In situ CD measurement of 432 helicoid II (b) In situ CD measurement when T20 molecule was inserted at 0 min (c) at 40 min (d) at 80 min

The maximum dissymmetry factor regardless of peak positions respect to the reaction time has been plotted in figure 3.11 to more clearly show the progressive increase of chiroptic response. While introduction of T20 at 80 minutes after reaction started, no significant change of the final dissymmetric factor nor chirality evolution kinetic was observed. Upon addition of T20 after 40 minutes since reaction started, slight increase of final chiroptical response was observed. Interestingly, addition of T20 at the beginning of the reaction shows significant increase of chiroptical response, with more steep incline of chirality evolution. From this time resolved study, the involvement of T20 at the early stage of the growth shows most significant influence on the final chiroptic response. As the first 40 minutes of the reaction is devoted to achiral high-index generation, it is possible to expect that T20 molecule is mostly related with development or stabilization of high-index facets.

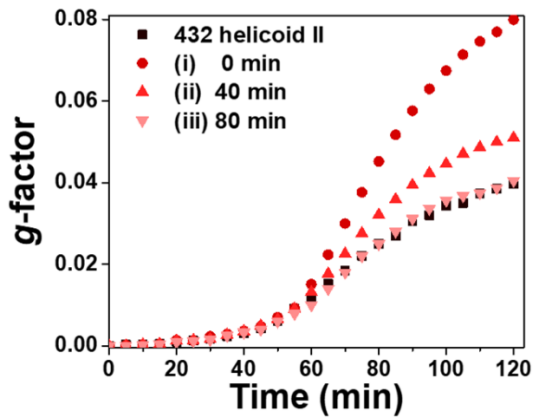

Figure 3.11 Change of g-factor of 432 helicoid II and newly synthesized 432 helicoid II with T20 molecules respect to reaction time depending on the insertion time.

The exact role of T20 during the early stage of 432 helicoid II synthesis could be understood by difference in binding affinity between T20 and glutathione molecules respect to gold surface.[97-103] While glutathione molecules are known to interact with gold surface through thiol group to form a strong chemical bond, thymine base of T20 interact with gold surface by keto group of pyrimidine ring via physisorption force. Considering chemisorption generally show stronger interaction force compared to that of physisorption, dominant effect of glutathione on chiral evolution could be expected. However, despite relatively weaker interaction with the gold surface, T20 could significantly influence the nanoparticle growth pathway. Previously, we have shown that change in seed morphology could induce significantly different growth pathway, indicating, small changes in the initial growth stage during chiral evolution serves as critical factor to final chiroptic response.[87] While the detailed mechanism of T20 interaction with gold surface while presence of the glutathione molecule in 432 helicoid II synthesis condition still requires further study, experimental results show that T20 can affect the growth pathway of chirality evolution. Therefore, devised synthetic method holds significance as the first attempt to precisely tune chiroptic response using oligonucleotide, and further sequence dependent study is expected to expand the accessible nanophotonic designs.

3.4 Conclusion

The introduction of biomolecular oligonucleotides into chiral 432 helicoid III nanoparticles has been studied to control their optical properties. In order to make the nucleic acid molecules conjugate well to the gold nanosurface, a strategy of adding thiol having high affinity to gold at the end of the oligonucleotide was used. Also, chirality enhancement of chiral 432 helicoid II nanoparticle using multiple bio-molecular additive has been demonstrated using T20 oligonucleotide and glutathione molecules. Newly synthesized 432 helicoid II with T20 shows twofold increase of dissymmetric factor compared to previous 432 helicoid II under specific concentration ratio between glutathione and T20. Additionally, time resolved analysis of growth pathway was conducted to understand the involvement of T20 on the enhancement of chiroptic response. T20 shows most effective chirality evolution when inserted to the growth solution from the initial growth stage, stating involvement in high-index and chiral motif generation regime. We envision that presented chiralitymodified synthetic method provides a glimpse to vast expansion of chiral metamaterials for versatile applications.

Chapter 4. Nucleic acid-assisted synthesis of gold nanoparticles for plasmonic chiroptical amplification

4.1 Introduction

Nucleic acids are molecules that enable organisms to transfer genetic information from generation to generation. These macromolecules store the genetic information that determines traits and enables protein synthesis. Nucleic acid consists of phosphate backbone, pentose sugar, and base. The pentose sugar of DNA is deoxyribose, and the pentose sugar of RNA is ribose, and the diene has bases of adenine, guanine, cytosine, and thymine. RNA has uracil base instead of thymine. After the discovery of a particular DNA structure by Watson and Crick in the 1950s, [104] scientists no longer viewed nucleic acid molecules as a medium for storing or transmitting genetic information, but as a material for creating novel structures. In the meantime, the field of artificial synthesis of nucleic acids has also undergone rapid development, and now the oligonucleotide sequence is easily available.

Research on the interaction of nucleic acid molecules with gold has been actively conducted.[97,98,105,106] Many studies have attempted to induce the interaction of gold and nucleic acid molecules by adding thiol modifications at the 5' or 3' ends of the nucleic acid sequences, or by adding phosphorothioate modifications that produce sulfur atoms in their backbones.[105] The affinity for the gold surface of the nucleobase itself, without any thiol modification, has also been reported. In these papers, the affinity on the gold surface was reduced in the order of adenine, cytosine, guanine and thymine.[97]

Also researches on nanostructure fabrication using these interactions has been actively conducted. First, in terms of nanoparticle assembly, DNA origami technology is one of the technologies that drove the development of DNA nanotechnology as a whole.[107] It is a technology that folds and fixes long strands of DNA extracted from viruses into dozens to hundreds of short DNA strands to form desired structures. Various assembly studies have been reported using this technique, including chiral arrays of gold nanoparticles.[108,109] In addition, there have been cases where the biocompatibility of nucleic acid molecules has been combined with nanoparticles and used in the biomedical fields.[110,111] There have been studies on nanoparticle growth that take advantage of the different affinity for gold in nucleobases to grow into different morphologies depending on the sequence added.[93]

We set up a strategy to induce chiral morphology by introducing these attractive biomaterials, nucleic acids into gold nanoparticle growth. This adds the inherent advantages of nucleic acid molecules to the optical properties of gold nanoparticles. When the distinct affinity of nucleobases and the distinct chirality of deoxyribose and ribose are applied, a new synthesis systems with high versatility could be developed. Previous studies with similar strategies and intentions exist, but they are either achiral nanoparticles arranged to be chiral with nucleic acid molecules or nucleic acid molecules are involved in nanoparticle growth to generate achiral morphologies.

4.2 Synthesis of oligonucleotide-assisted chiral gold nanoparticles

We have expanded our seed-mediated growth using organothiols, based on our experience in synthesizing 3D nanostructures with morphologies that have never been reported before and unique optical properties, and induced chirality in the morphology of the resulting nanoparticles by introducing nucleic acid molecules into the secondary growth solution. A schematic diagram of the synthesis process for oligonucleotide-assisted chiral gold nanoparticles is shown in the figure 4.1. First, gold octahedral nanoparticles are synthesized using a seed-mediated growth method. The octahedrons grow again in growth solutions containing gold precursors, reducing agents, surfactants and oligonucleotide molecules.

Chemicals

Tetrachloroauric(iii) trihydrate ($HAuCl_4 3H_2O$, 99.9%), Sodium borohydride ($NaBH_4$, 99%), Hexadecyltrimethylammonium bromide (CTAB, 99%), L-glutathione (γ-EC-G, 98%) and L-ascorbic acid (99%) were purchased from Sigma-Aldrich and were used without further purification. Oligonucleotides were purchased from Integrated DNA Technologies. High-purity deionized (DI) water (18.2 MΩ cm) was used in all of the procedures.

Synthesis of Chiral Gold Nanoparticles

Au Nanocubes(AuNCs) with a 44 nm edge length were synthesized as previously reported.[65] First, small gold seeds (~2.5 nm) were prepared by the reduction of a $HAuCl_4 3H_2O$ aqueous solution (10 mM, 250 μl) with a $NaBH_4$ aqueous solution (10 mM, 800 μl) in a CTAB aqueous solution (100 mM, 7.5 ml). The gold seeds were added to the growth solution consisting of a $HAuCl_4 3H_2O$ aqueous solution (10 mM, 200 μl), a CTAB aqueous solution (100 mM, 1.6 mL), and an ascorbic acid solution (100 mM, 950μl). After 15 min, the synthesized AuNCs were washed by centrifugation (10000 rpm, 60 s) and dispersed in deionized water.AuNCs were centrifuged (6,708g, 150s) twice and dispersed in CTAB (1 mM) solution. The growth solution for chiral Helicoid II nanoparticles was prepared by adding 800 μl of 100mMCTAB and 200 μl of 10mM gold chloride trihydrate into 3.95ml of deionized waterto form an $[AuBr_4]^-$ complex. Au^{3+} was then reduced by the rapid injection of 475 μl of 100mM ascorbic acid solution. The growth of chiral nanoparticles was initiated by adding L-glutathione solution and AuNC solution intothe growth solution. For the preparation of programmed Helicoid II nanoparticles, T20 oligonucleotide solution (in Tris-EDTA buffer, 500 nM) was additionally added.

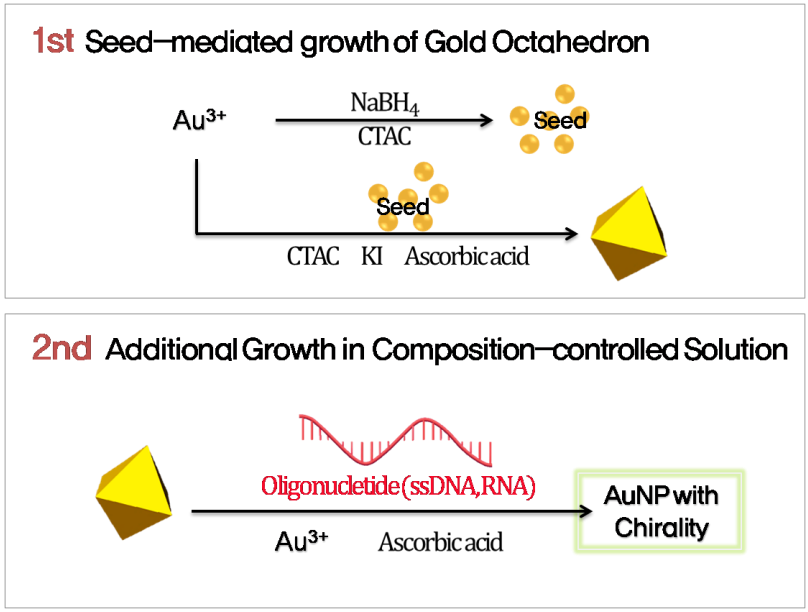

Figure 4.1 Schematic of growth procedure for oligonucleotide-assisted chiral gold nanoparticles

4.3 Factors affecting chiroptical responses of oligonucleotide-assisted gold nanoparticles

Sequences of oligonucleotides

Kuhn's dis-symmetry factor (g-value) is a dimensionless value which is useful for quantitative comparisons of chiroptic responses among different systems and was calculated from the measured extinction and CD values using $g - \text{value} = \frac{2(A_L - A_R)}{A_L + A_R} \propto \frac{\text{CD}}{\text{extinction}}$. When synthesized using three sequences of homooligonucleotide adenine 20 mer, thymine 20 mer, and cytosine 20 mer, chirality was expressed in the resulting nanoparticles only when adenine-containing sequences were used. (figure 4.2) The g -value was observed to be a maximum of 0.02. In the case of thymine and cytosine, there was no chiral expression in the result at all concentrations.

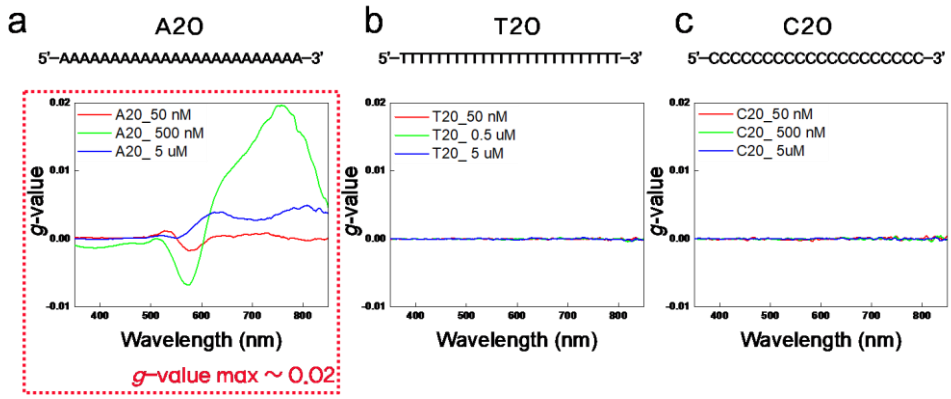

Figure 4.2 Sequence-dependent chiroptical responses of oligonucleotide-assisted chiral gold nanoparticles. *g*-value spectra of resultant particles using oligonucleotide sequences of (a) A20 (b) T20 and (c) C20

The synthesis was conducted by adjusting only the content of adenine in the 20-mer sequence of the same length. From the T20 without adenine at all, 20 mer sequences consisting of 1, 5, 10, 19, and 20 increased adenine were used. After the synthesis, circular dichroism was measured and chirality was also observed in sequences other than the A20 sequence. Synthesis was conducted for the final oligonucleotide concentrations of 50 nM, 500 nM, and 5 uM. A graph of the *g*-value of the adenine contents in the sequence is shown in figure 4.3. When it began to contain more than 5 adenine bases, chiroptic activity began to appear and reached maximum *g*-value in adenine 20mer. Here, we found that adenine bases play an essential role in chirality when introducing single-stranded oligonucleotides of 20-mer length sequences into the growth process of gold nanoparticles.

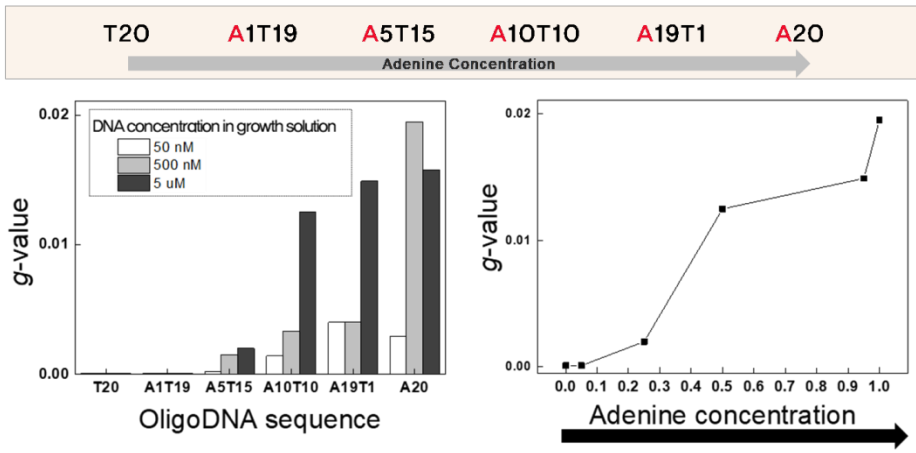

Figure 4.3 Changes in *g*-values of synthesized nanoparticles according to adenine proportions in 20 mer length oligonucleotide sequences containing adenine and thymine.

After confirming that the adenine bases in these sequences and the chiroptical activity of the resulting gold nanoparticles are closely related, how the chiroptical properties change when the sequence forms a pattern including adenine has been tested. In order to compare various patterns efficiently, we tried to use oligonucleotide molecues of 12 mer with many common divisors. We have designed a total of twelve patternde sequences with several criterias, such as the number of consecutive adenine bases, the total number of adenine bases, the number of cytosine bases between adenine bases, and the length of the repeating patterns. (table 4.1)

	Number of consecutive A's	Total number of A	Number of C between A	The length of the repeating pattern (number of A in one pattern)
ACACACACACAC	1	6	1	2(1)
ACCACCACCACC	1	4	2	3(1)
ACCCACCCACCC	1	3	3	4(1)
ACCCCCACCCCC	1	2	5	6(1)
AACAACAACAAC	2	8	1	3(2)
AACCAACCAACC	2	6	2	4(2)
AACCCCAACCCC	2	4	4	6(2)
AAACAAACAAAC	3	9	1	4(3)
AAACCCAAACCC	3	6	3	6(3)
AAAACCAAAACC	4	8	2	6(4)
AAAAACAAAAAC	5	10	1	6(5)
AAAAAAAAAAAA	12	12		

Table 4.1 A list of 12 mer sequences consisting of adenine and cytosine using in the synthesis process of oligonucleotide-assisted chiral nanoparticles. The 12 mer oligonucleotide sequences were patterned according to several criteria including the number of consecutive adenine bases, the total number of adenine bases, the number of cytosine bases between adenine bases, and the length of the repeating patterns.

As a result of the experiment, It was different from the previous experiment. When the twelve sequences containing anenin had some patterns, simply the total number of adenine in the sequence was no longer proportional to the chiroptical activity of the resulting nanoparticles. For example, a sequence of four repeated ‘AAC’s may be compared to a sequence of two repeated ‘AAAACC’s. The total number of adenine was equal to 8, but the difference was shown in g value and spectrum shape. Figure 4.4 shows the change of g-value of synthesized nanoparticles according to the total number of adenine in the 12 mer oligonucleotide sequences. Through these results, we could foresee the possibility of increasing the chirality of the resulting nanoparticles through various carefully programmed patterning processes.

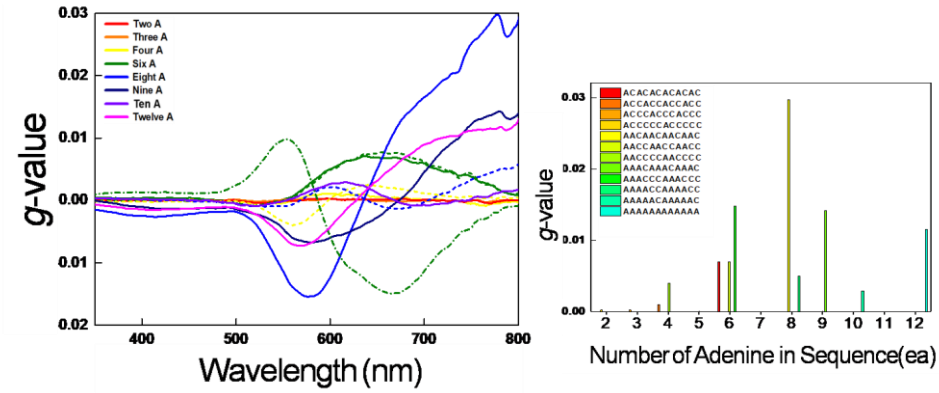

Figure 4.4 Change of *g*-value of synthesized nanoparticles according to the total number of adenine in the 12 mer oligonucleotide sequences.

In this experiment, the highest *g*-values were found, especially for the 12 mer sequences with four repeated 'AAC' patterns. This was a chiroptical activity three times larger than the 12 mer sequence, where only 12 adenines were repeated. Figure 4.5 shows *g*-value spectra of synthesized chiral gold nanopaticles when using oligonucleotide sequences 5'-AACAACAACAAC-3' and 5'-AAAAAAAAAAAA-3'. In case of 5'-AAAAAAAAAAAA-3', the maximum value of *g*-value was 0.013, while in case 5'-AACAACAACAAC-3', the maximum value of *g*-value was 0.032. We have found in the previous experiment that adenine in the oligonucleotide sequence plays an important role in the chiroptical properties of the resulting nanoparticles. However, as in this case, the chiroptical response was measured even at a lower adenine level. It is certain that the interaction between the gold nanoparticle surface and the adenine base is involved, but that does not necessarily mean that greater chirality of resultant nanoparticle is expressed when the interaction is large. Perhaps the more complex and subtle interactions between the gold surface and the nucleobases and the three-dimensional structure of the nucleic acid during nanoparticle growth is involved. Further experimentation and analysis will be needed to make this clearer.

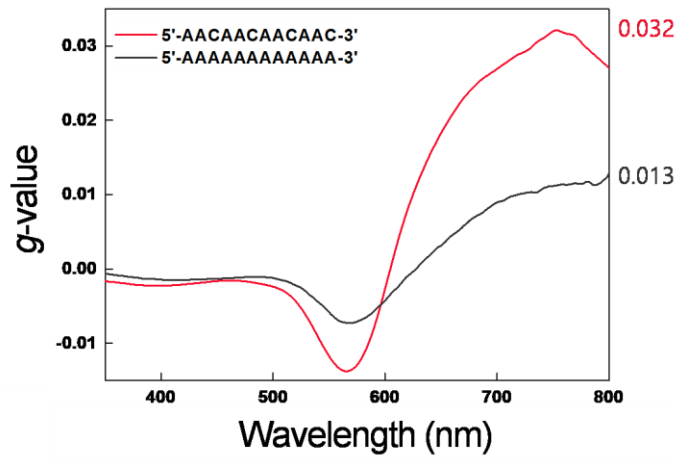

Figure 4.5 *g*-value spectra of synthesized chiral gold nanopaticles when using oligonucleotide sequences 5'-AACAACAACAAC-3' and 5'-AAAAAAAAAAAA-3'.

Gold precursor concentration

Further experiments using 5'-AACAACAACAAC-3' oligonucleotide sequences were conducted. Figure 4.6 shows Change in properties of synthesized gold nanoparticles according to the concentration of gold precursor in the growth solution. Spectra of *g*-value (b) extinction and (c) the SEM images for the corresponding gold precursor concentrations. First, the precursor concentration of the growth solution was adjusted. As the concentration of precursor in solution changes, the resulting nanoparticles show chiroptical activity and extinction at different wavelengths in the visible region. (figure 4.6a and b) We also observed SEM image for each sample.(figure 4.6c) In the case of the 200 μM gold precursor concentration with the largest chirality, the four-branched petal-like structure was evident. In addition, the cases of molar concentrations of 125 uM and 150 uM, which were identified with a value of more than 0.01, also showed these four separate shapes in the resulting nanoparticles. However, as the gold precursor concentration increased from 200 uM to 300 and 500 uM, the nanoparticle size became larger and the four-furcated bent shape was no longer confirmed. As a result, *g*-values were measured at a sharply lower level.

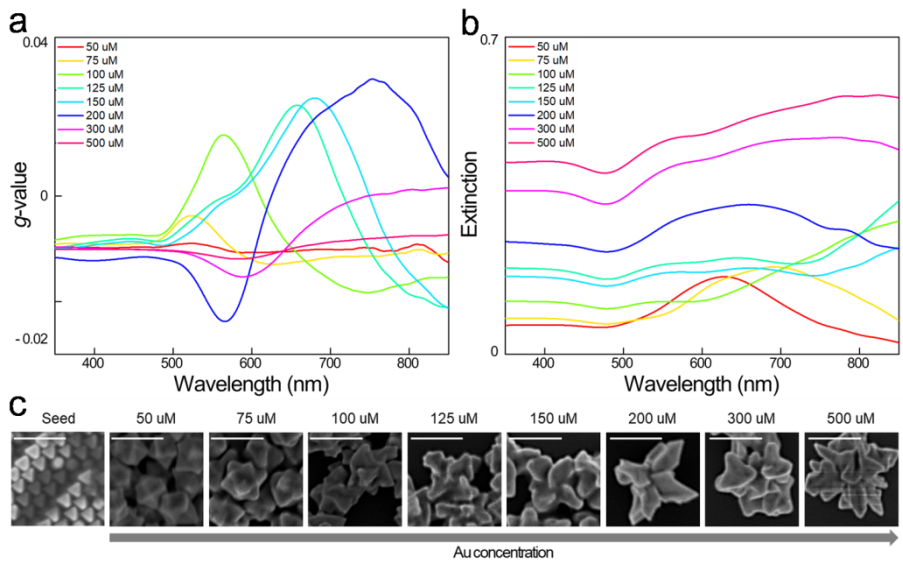

Figure 4.6 Change in properties of synthesized gold nanoparticles according to the concentration of gold precursor in the growth solution. Spectra of (a) *g*-value (b) extinction and (c) the SEM images for the corresponding gold precursor concentrations

4.4 Time-dependent observation for oligonucleotide-assisted chiral gold nanoparticles

In order to observe the expression of chirality over time in real time, we conducted *in situ* measurement in the nanoparticle synthesis process. Circular dichroism(CD) spectra were obtained using a J-815 spectropolarimeter instrument (JASCO). For the real-time observation of chirality development of nanoparticles, *in-situ* CD measurement was conducted. Synthesis of chiral nanoparticles was performed inside the CD instrument, and the CD was measured 24 times, once every 5 minutes. Figure 4.7 shows the time-dependent chirality development of oligonucleotide-assisted chiral gold nanoparticles. Figure 4.7a shows *in situ* measurement of circular dichroism and 4.7b shows the *in situ* measurement of extinction for nanoparticle growth. An interesting fact from the real time measurements was that the CD spectrum changes very dynamically as the chirality of the nanoparticles develops. After 55 minutes, a new negative peak in the mid 500 nanometer region emerges. After 70 minutes, the shape remained negative in the 500 nanometer range and in the positive direction in the 700 nanometer range, and its intensity increased until 120 minutes.

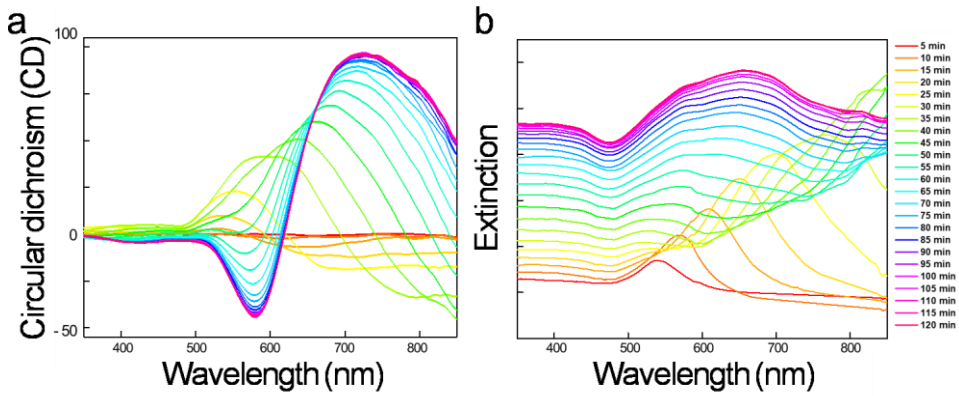

Figure 4.7 Observation of time-dependent chirality development of oligonucleotide-assisted chiral gold nanoparticles. *In situ* measurement of (a) circular dichroism and (b) extinction for nanoparticle growth

In order to explore this radical change, we observed the growth of nanoparticles over reaction time by SEM observation. Figure 4.8 shows SEM images of synthesized gold nanoparticles for the corresponding reaction time in figure 4.7. For morphological observation over time, the same growth solution was divided into 12 parts and the growth time was cut at 10 minute intervals from 10 minutes to 120 minutes. The observations were as follows: At about 10 minutes, it was in the form of a high-index nanoparticle, which does not show much chirality. As time went by, it developed into a trisoctahedron form with chirality, and after 60 minutes, it changed into a four branched and curved petal form. 70 minutes after the start of the reaction, the nanoparticles maintained a four-pronged outline, showing an overall increase in size and only partial changes. It was understood that this large change in shape and size in the middle stage affected the rapid spectral shape change of the in situ CD spectrum measured in real time.

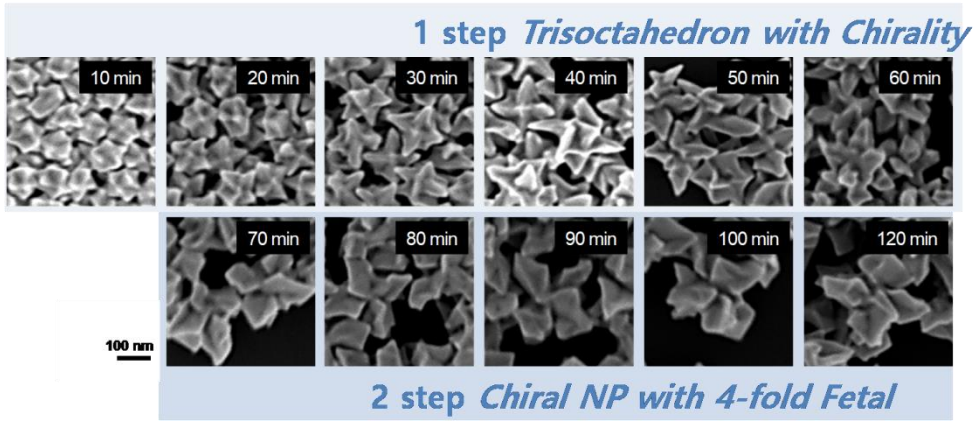

Figure 4.8 SEM images of synthesized gold nanoparticles for the corresponding reaction time in figure 4.7.

4.5 Conclusion

Since the unique structure was discovered by Watson and Crick, scientists no longer viewed nucleic acid molecules as a medium for storing or transmitting genetic information, but as a material for creating novel nanostructures. We have expanded our seed-mediated growth using organothiols, based on our experience in synthesizing nanostructures with morphologies that have never been reported before and unique optical properties, and induced chirality in the morphology of the resulting nanoparticles by introducing nucleic acid molecules into the secondary growth solution. Chiral gold nanoparticles were synthesized using a strategy of introducing oligonucleotide molecules into the seed-mediated growth process of gold octahedron. Different chiroptical activities were expressed in the gold nanoparticles depending on the nucleotide sequences and time-dependent chirality development was observed by *in situ* CD measurement.

Chapter 5. Concluding remarks

In a concluding manner, we describe the significance found in the thesis. As a strategy to introduce organic molecules such as organothiols and nucleic acids into the seed-mediated growth process of gold nanoparticles, the shape at the nanoscale was controlled and the optical signal amplification was confirmed. The new nanostructure synthesis system presented in this thesis is simple, adaptable, and adds programmability and diversity to synthetic process. As a result, the new nanostructures thus synthesized could be effectively used for Raman scattering and amplification of circular dichroism signals.

References

1 Brady, P. & Cummings, M. Natural History Note Differential Response To Circularly Polarized Light By The Jewel Scarab Beetle Chrysina Gloriosa. *The American Naturalist* **175**, 7 (2010).

2 Rosi, N. L. & Mirkin, C. A. Nanostructures in Biodiagnostics. *Chemical Reviews* **105**, 1547-1562, doi:10.1021/cr030067f (2005).

3 Kelly, K. L., Coronado, E., Zhao, L. L. & Schatz, G. C. The Optical Properties of Metal Nanoparticles: The Influence of Size, Shape, and Dielectric Environment. *The Journal of Physical Chemistry B* **107**, 668-677, doi:10.1021/jp026731y (2003).

4 Kan, T. Y., Song, H. & Kim, K. Localized Plasmon Phenomenon Using Nanostructures and Its Applications. *Polymer Science and Technology* **26**, 5 (2015).

5 Jans, H. & Huo, Q. Gold nanoparticle-enabled biological and chemical detection and analysis. *Chemical Society Reviews* **41**, 2849-2866, doi:10.1039/C1CS15280G (2012).

6 Hao, E. & Schatz, G. C. Electromagnetic fields around silver nanoparticles and dimers. *J. Chem. Phys.* **120** (2004).

7 Prakash, J., Swart, H. C., Zhang, G. & Sun, S. Emerging applications of atomic layer deposition for the rational design of novel nanostructures for surface-enhanced Raman scattering. *Journal of Materials Chemistry C* **7**,

1447-1471, doi:10.1039/C8TC06299D (2019).

8 Chung, T., Lee, S.-Y., Song, E. Y., Chun, H. & Lee, B. Plasmonic nanostructures for nano-scale bio-sensing. *Sensors (Basel)* **11**, 10907-10929, doi:10.3390/s111110907 (2011).

9 Imbraguglio, D., Giovannozzi, A. & Rossi, A. Nanometrology. **185**, 193-220, doi:10.3254/978-1-61499-326-1-193 (2013).

10 Turkevich, J., Stevenson, P. C. & Hillier, J. A study of the nucleation and growth processes in the synthesis of colloidal gold. *Discussions of the Faraday Society* **11**, 55-75, doi:10.1039/DF9511100055 (1951).

11 Jana, N. R., Gearheart, L. & Murphy, C. J. Wet Chemical Synthesis of High Aspect Ratio Cylindrical Gold Nanorods. *The Journal of Physical Chemistry B* **105**, 4065-4067, doi:10.1021/jp0107964 (2001).

12 Nikoobakht, B. & El-Sayed, M. A. Preparation and Growth Mechanism of Gold Nanorods (NRs) Using Seed-Mediated Growth Method. *Chemistry of Materials* **15**, 1957-1962, doi:10.1021/cm020732l (2003).

13 Niu, W., Zhang, L. & Xu, G. Seed-mediated growth of noble metal nanocrystals: crystal growth and shape control. *Nanoscale* **5**, 3172-3181, doi:10.1039/C3NR00219E (2013).

14 Raman, C. V. & Krishnan, K. S. A New Type of Secondary Radiation. *Nature* **121**, 501-502, doi:10.1038/121501c0 (1928).

15 Jang, E.-S. A Review of SERS for Biomaterials Analysis Using Metal Nanoparticles. *Ceramist*

22 (2019).

16 Aroca, R. *Surface- Enhanced Vibrational Spectroscopy*. (Wiley, 2006).

17 Fleischmann, M., Hendra, P. J. & McQuillan, A. J. Raman spectra of pyridine adsorbed at a silver electrode. *Chemical Physics Letters* **26**, 163-166 (1974).

18 Unser, S., Bruzas, I., He, J. & Sagle, L. Localized Surface Plasmon Resonance Biosensing: Current Challenges and Approaches. *Sensors* **15** (2015).

19 Willets, K. A. & Duyne, R. P. V. Localized Surface Plasmon Resonance Spectroscopy and Sensing. *Annu. Rev. Phys. Chem.* **58**, 267-297 (2007).

20 Jeong, H.-H. *et al.* Dispersion and shape engineered plasmonic nanosensors. *Nature Communications* **7** (2016).

21 Jeong, H.-H., Mark, A. G. & Fischer, P. Magnesium plasmonics for UV applications and chiral sensing. *Chemical Communications* **52**, 12179-12182, doi:10.1039/C6CC06800F (2016).

22 Matuschek, M. *et al.* Chiral Plasmonic Hydrogen Sensors. *Small* **14**, 1702990 (2018).

23 Hendry, E. *et al.* Ultrasensitive detection and characterization of biomolecules using superchiral fields. *Nature Nanotechnology* **5**, 783, doi:10.1038/nnano.2010.209 (2010).

24 Kelly, C. *et al.* Chiral Plasmonic Fields Probe Structural Order of Biointerfaces. *Journal of the American Chemical Society* **140**, 8509-8517,

doi:10.1021/jacs.8b03634 (2018).

25 Rodier, M. *et al.* Probing Specificity of Protein–Protein Interactions with Chiral Plasmonic Nanostructures. *The Journal of Physical Chemistry Letters* **10**, 6105-6111, doi:10.1021/acs.jpclett.9b02288 (2019).

26 Tullius, R. *et al.* Superchiral Plasmonic Phase Sensitivity for Fingerprinting of Protein Interface Structure. *ACS Nano* **11**, 12049-12056, doi:10.1021/acsnano.7b04698 (2017).

27 Bochenkov, V. E. & Sutherland, D. S. Chiral plasmonic nanocrescents: large-area fabrication and optical properties. *Opt. Express* **26**, 27101-27108, doi:10.1364/OE.26.027101 (2018).

28 Le, K. Q., Hashiyada, S., Kondo, M. & Okamoto, H. Circularly Polarized Photoluminescence from Achiral Dye Molecules Induced by Plasmonic Two-Dimensional Chiral Nanostructures. *The Journal of Physical Chemistry C* **122**, 24924-24932, doi:10.1021/acs.jpcc.8b07297 (2018).

29 Tian, X., Fang, Y. & Zhang, B. Multipolar Fano Resonances and Fano-Assisted Optical Activity in Silver Nanorice Heterodimers. *ACS Photonics* **1**, 1156-1164, doi:10.1021/ph5002457 (2014).

30 Zu, S., Bao, Y. & Fang, Z. Planar plasmonic chiral nanostructures. *Nanoscale* **8**, 3900-3905, doi:10.1039/C5NR09302C (2016).

31 Cao, T. *et al.* Fano Resonance in Asymmetric Plasmonic Nanostructure: Separation of Sub- 10 nm Enantiomers. *Advanced optical materials* **7** (2019).

32 Han, T. *et al.* Reveal and Control of Chiral Cathodoluminescence at Subnanoscale. *Nano Letters* **18**, 567-572, doi:10.1021/acs.nanolett.7b04705 (2018).

33 Zu, S. *et al.* Deep-Subwavelength Resolving and Manipulating of Hidden Chirality in Achiral Nanostructures. *ACS Nano* **12**, 3908-3916, doi:10.1021/acsnano.8b01380 (2018).

34 García-Guirado, J., Svedendahl, M., Puigdollers, J. & Quidant, R. Enantiomer-Selective Molecular Sensing Using Racemic Nanoplasmonic Arrays. *Nano Letters* **18**, 6279-6285, doi:10.1021/acs.nanolett.8b02433 (2018).

35 Kuppe, C. *et al.* Measuring optical activity in the far-field from a racemic nanomaterial: diffraction spectroscopy from plasmonic nanogratings. *Nanoscale Horizons*, doi:10.1039/C9NH00067D (2019).

36 Zhao, Y. *et al.* Shell-Engineered Chiroplasmonic Assemblies of Nanoparticles for Zeptomolar DNA Detection. *Nano Letters* **14**, 3908-3913, doi:10.1021/nl501166m (2014).

37 Lee, H. E., Ahn, H. Y., Lee, J. & Nam, K. T. Biomolecule- Enabled Chiral Assembly of Plasmonic Nanostructures. *ChemNanoMat* **3** (2017).

38 Wu, X. *et al.* Unexpected Chirality of Nanoparticle Dimers and Ultrasensitive Chiroplasmonic Bioanalysis. *Journal of the American Chemical Society* **135**, 18629-18636, doi:10.1021/ja4095445 (2013).

39 Cai, J. *et al.* Chiral Shell Core–Satellite Nanostructures for Ultrasensitive

Detection of Mycotoxin. *Small* **14**, 1703931 (2018).

40 Kumar, J. *et al.* Detection of amyloid fibrils in Parkinson's disease using plasmonic chirality. *PNAS* **115**, 3225-3230 (2018).

41 Schlücker, S. Surface- Enhanced Raman Spectroscopy: Concepts and Chemical Applications. *Angew. Chem.* **53** (2014).

42 Zhang, Y. *et al.* Rapid simultaneous detection of multi-pesticide residues on apple using SERS technique. *Analyst* **139**, 5148-5154, doi:10.1039/C4AN00771A (2014).

43 Cheng, Z. *et al.* Simultaneous Detection of Dual Prostate Specific Antigens Using Surface-Enhanced Raman Scattering-Based Immunoassay for Accurate Diagnosis of Prostate Cancer. *ACS Nano* **11**, 4926-4933, doi:10.1021/acsnano.7b01536 (2017).

44 Xie, W., Walkenfort, B. & Schlücker, S. Label-Free SERS Monitoring of Chemical Reactions Catalyzed by Small Gold Nanoparticles Using 3D Plasmonic Superstructures. *Journal of the American Chemical Society* **135**, 1657-1660, doi:10.1021/ja309074a (2013).

45 Romo-Herrera, J. M. *et al.* A study of the depth and size of concave cube Au nanoparticles as highly sensitive SERS probes. *Nanoscale* **8**, 7326-7333, doi:10.1039/C6NR01155A (2016).

46 Chang, H. *et al.* Synthesis of optically tunable bumpy silver nanoshells by changing the silica core size and their SERS activities. *RSC Advances* **7**, 40255-40261, doi:10.1039/C7RA06170F (2017).

47 Zhang, G., Li, J., Shen, A. & Hu, J. Synthesis of size-tunable chitosan encapsulated gold–silver nanoflowers and their application in SERS imaging of living cells. *Physical Chemistry Chemical Physics* **17**, 21261-21267, doi:10.1039/C4CP05343E (2015).

48 Zhang, Q., Large, N. & Wang, H. Gold Nanoparticles with Tipped Surface Structures as Substrates for Single-Particle Surface-Enhanced Raman Spectroscopy: Concave Nanocubes, Nanotrisoctahedra, and Nanostars. *ACS Applied Materials & Interfaces* **6**, 17255-17267, doi:10.1021/am505245z (2014).

49 Nie, S. & Emory, S. R. Probing Single Molecules and Single Nanoparticles by Surface-Enhanced Raman Scattering. *Science* **275**, 1102, doi:10.1126/science.275.5303.1102 (1997).

50 Talley, C. E. *et al.* Surface-Enhanced Raman Scattering from Individual Au Nanoparticles and Nanoparticle Dimer Substrates. *Nano Letters* **5**, 1569-1574, doi:10.1021/nl050928v (2005).

51 Khoury, C. G. & Vo-Dinh, T. Gold Nanostars For Surface-Enhanced Raman Scattering: Synthesis, Characterization and Optimization. *The Journal of Physical Chemistry C* **112**, 18849-18859, doi:10.1021/jp8054747 (2008).

52 Dandapat, A. *et al.* Attomolar Level Detection of Raman Molecules with Hierarchical Silver Nanostructures Including Tiny Nanoparticles between Nanosized Gaps Generated in Silver Petals. *ACS Applied Materials &*

Interfaces **7**, 14793-14800, doi:10.1021/acsami.5b03109 (2015).

53 Liu, X., Osada, M., Kitamura, K., Nagata, T. & Si, D. Ferroelectric-assisted gold nanoparticles array for centimeter-scale highly reproducible SERS substrates. *Scientific Reports* **7**, 3630, doi:10.1038/s41598-017-03301-y (2017).

54 Lee, J. *et al.* Capillary Force-Induced Glue-Free Printing of Ag Nanoparticle Arrays for Highly Sensitive SERS Substrates. *ACS Applied Materials & Interfaces* **6**, 9053-9060, doi:10.1021/am5000382 (2014).

55 Schweikart, A., Pazos-Pérez, N., Alvarez-Puebla, R. A. & Fery, A. Controlling inter-nanoparticle coupling by wrinkle-assisted assembly. *Soft Matter* **7**, 4093-4100, doi:10.1039/C0SM01359E (2011).

56 Baik, J. M., Lee, S. J. & Moskovits, M. Polarized Surface-Enhanced Raman Spectroscopy from Molecules Adsorbed in Nano-Gaps Produced by Electromigration in Silver Nanowires. *Nano Letters* **9**, 672-676, doi:10.1021/nl803145d (2009).

57 Tao, C.-a. *et al.* Cucurbit[n]urils as a SERS hot-spot nanocontainer through bridging gold nanoparticles. *Chemical Communications* **47**, 9867-9869, doi:10.1039/C1CC12474A (2011).

58 Li, W., Camargo, P. H. C., Lu, X. & Xia, Y. Dimers of Silver Nanospheres: Facile Synthesis and Their Use as Hot Spots for Surface-Enhanced Raman Scattering. *Nano Letters* **9**, 485-490, doi:10.1021/nl803621x (2009).

59 Roy, S., Ajmal, C. M., Baik, S. & Kim, J. Silver nanoflowers for single-

particle SERS with 10 pM sensitivity. *Nanotechnology* **28** (2017).

60 Lin, H.-X. *et al.* Uniform gold spherical particles for single-particle surface-enhanced Raman spectroscopy. *Physical Chemistry Chemical Physics* **15**, 4130-4135, doi:10.1039/C3CP43857K (2013).

61 Kang, H. *et al.* One-step synthesis of silver nanoshells with bumps for highly sensitive near-IR SERS nanoprobes. *Journal of Materials Chemistry B* **2**, 4415-4421, doi:10.1039/C4TB00442F (2014).

62 Chang, H. *et al.* Ag Shell–Au Satellite Hetero-Nanostructure for Ultra-Sensitive, Reproducible, and Homogeneous NIR SERS Activity. *ACS Applied Materials & Interfaces* **6**, 11859-11863, doi:10.1021/am503675x (2014).

63 Chikkaraddy, R. *et al.* How Ultranarrow Gap Symmetries Control Plasmonic Nanocavity Modes: From Cubes to Spheres in the Nanoparticle-on-Mirror. *ACS Photonics* **4**, 469-475, doi:10.1021/acsphotonics.6b00908 (2017).

64 McLellan, J. M., Li, Z.-Y., Siekkinen, A. R. & Xia, Y. The SERS Activity of a Supported Ag Nanocube Strongly Depends on Its Orientation Relative to Laser Polarization. *Nano Letters* **7**, 1013-1017, doi:10.1021/nl070157q (2007).

65 Ahn, H.-Y., Lee, H.-E., Jin, K. & Nam, K. T. Extended gold nano-morphology diagram: synthesis of rhombic dodecahedra using CTAB and ascorbic acid. *Journal of Materials Chemistry C* **1**, 6861-6868,

doi:10.1039/C3TC31135J (2013).

66 Lee, H.-E. *et al.* Concave Rhombic Dodecahedral Au Nanocatalyst with Multiple High-Index Facets for CO2 Reduction. *ACS Nano* **9**, 8384-8393, doi:10.1021/acsnano.5b03065 (2015).

67 Wu, H.-L., Kuo, C.-H. & Huang, M. H. Seed-Mediated Synthesis of Gold Nanocrystals with Systematic Shape Evolution from Cubic to Trisoctahedral and Rhombic Dodecahedral Structures. *Langmuir* **26**, 12307-12313, doi:10.1021/la1015065 (2010).

68 Häkkinen, H. The gold–sulfur interface at the nanoscale. *Nature Chemistry* **4**, 443-455, doi:10.1038/nchem.1352 (2012).

69 Yamamuro, S. & Sumiyama, K. Why do cubic nanoparticles favor a square array? Mechanism of shape-dependent arrangement in nanocube self-assemblies. *Chemical Physics Letters* **418**, 166-169, (2006).

70 Liu, X. *et al.* Effect of Growth Temperature on Tailoring the Size and Aspect Ratio of Gold Nanorods. *Langmuir* **33**, 7479-7485, doi:10.1021/acs.langmuir.7b01635 (2017).

71 Lombardi, A. *et al.* Anomalous Spectral Shift of Near- and Far-Field Plasmonic Resonances in Nanogaps. *ACS Photonics* **3**, 471-477, doi:10.1021/acsphotonics.5b00707 (2016).

72 Benz, F. *et al.* SERS of Individual Nanoparticles on a Mirror: Size Does Matter, but so Does Shape. *The Journal of Physical Chemistry Letters* **7**, 2264-2269, doi:10.1021/acs.jpclett.6b00986 (2016).

73 Huang, Y.-F. *et al.* Surface-enhanced Raman spectroscopic study of p-aminothiophenol. *Physical Chemistry Chemical Physics* **14**, 8485-8497, doi:10.1039/C2CP40558J (2012).

74 Osawa, M., Matsuda, N., Yoshii, K. & Uchida, I. Charge transfer resonance Raman process in surface-enhanced Raman scattering from p-aminothiophenol adsorbed on silver: Herzberg-Teller contribution. *The Journal of Physical Chemistry* **98**, 12702-12707, doi:10.1021/j100099a038 (1994).

75 Hentschel, M., Schäferling, M., Duan, X., Giessen, H. & Liu, N. Chiral plasmonics. *Science Advances* **3**, e1602735, doi:10.1126/sciadv.1602735 (2017).

76 Saito, K. & Tatsuma, T. Chiral Plasmonic Nanostructures Fabricated by Circularly Polarized Light. *Nano Letters* **18**, 3209-3212, doi:10.1021/acs.nanolett.8b00929 (2018).

77 Liu, T. *et al.* Chiral Plasmonic Nanocrystals for Generation of Hot Electrons: Toward Polarization-Sensitive Photochemistry. *Nano Letters* **19**, 1395-1407, doi:10.1021/acs.nanolett.8b05179 (2019).

78 Yoo, S. & Park, Q.-H. Metamaterials and chiral sensing: a review of fundamentals and applications. *Nanophotonics* **8** (2019).

79 Urban, M. J. *et al.* Chiral Plasmonic Nanostructures Enabled by Bottom-Up Approaches. *Annual Review of Physical Chemistry* **70**, 275-299, doi:10.1146/annurev-physchem-050317-021332 (2019).

80 Frank, B. *et al.* Large-Area 3D Chiral Plasmonic Structures. *ACS Nano* **7**, 6321-6329, doi:10.1021/nn402370x (2013).

81 Yeom, B. *et al.* Chiral Plasmonic Nanostructures on Achiral Nanopillars. *Nano Letters* **13**, 5277-5283, doi:10.1021/nl402782d (2013).

82 Hentschel, M., Schäferling, M., Weiss, T., Liu, N. & Giessen, H. Three-Dimensional Chiral Plasmonic Oligomers. *Nano Letters* **12**, 2542-2547, doi:10.1021/nl300769x (2012).

83 Gansel, J. K. *et al.* Gold Helix Photonic Metamaterial as Broadband Circular Polarizer. *Science* **325**, 1513-1515, doi:10.1126/science.1177031 (2009).

84 Schreiber, R. *et al.* Chiral plasmonic DNA nanostructures with switchable circular dichroism. *Nature Communications* **4**, 2948, doi:10.1038/ncomms3948 (2013).

85 Karst, J. *et al.* Chiral Scatterometry on Chemically Synthesized Single Plasmonic Nanoparticles. *ACS Nano* **13**, 8659-8668, doi:10.1021/acsnano.9b04046 (2019).

86 Kuzyk, A. *et al.* DNA-based self-assembly of chiral plasmonic nanostructures with tailored optical response. *Nature* **483**, 311-314, doi:10.1038/nature10889 (2012).

87 Lee, H.-E. *et al.* Amino-acid- and peptide-directed synthesis of chiral plasmonic gold nanoparticles. *Nature* **556**, 360-365, doi:10.1038/s41586-018-0034-1 (2018).

88 Personick, M. L. & Mirkin, C. A. Making Sense of the Mayhem behind Shape Control in the Synthesis of Gold Nanoparticles. *Journal of the American Chemical Society* **135**, 18238-18247, doi:10.1021/ja408645b (2013).

89 Huang, X., Zhao, Z., Fan, J., Tan, Y. & Zheng, N. Amine-Assisted Synthesis of Concave Polyhedral Platinum Nanocrystals Having {411} High-Index Facets. *Journal of the American Chemical Society* **133**, 4718-4721, doi:10.1021/ja1117528 (2011).

90 Cho, N. H. *et al.* Cysteine Induced Chiral Morphology in Palladium Nanoparticle. *Particle & Particle Systems Characterization* **36** (2019).

91 Tan, L. H. *et al.* Mechanistic Insight into DNA-Guided Control of Nanoparticle Morphologies. *Journal of the American Chemical Society* **137**, 14456-14464, doi:10.1021/jacs.5b09567 (2015).

92 Wu, J. *et al.* DNA Sequence-Dependent Morphological Evolution of Silver Nanoparticles and Their Optical and Hybridization Properties. *Journal of the American Chemical Society* **136**, 15195-15202, doi:10.1021/ja506150s (2014).

93 Wang, Y., Satyavolu, N. S. R. & Lu, Y. Sequence-Specific Control of Inorganic Nanomaterials Morphologies by Biomolecules. *Curr Opin Colloid Interface Sci* **38**, 158-169, doi:10.1016/j.cocis.2018.10.009 (2018).

94 Ahn, H.-Y. *et al.* Bioinspired Toolkit Based on Intermolecular Encoder toward Evolutionary 4D Chiral Plasmonic Materials. *Accounts of*

Chemical Research **52**, 2768-2783, doi:10.1021/acs.accounts.9b00264 (2019).

95 Liu, B. & Liu, J. Methods for preparing DNA-functionalized gold nanoparticles, a key reagent of bioanalytical chemistry. *Analytical Methods* **9**, 2633-2643, doi:10.1039/C7AY00368D (2017).

96 Cutler, J. I., Auyeung, E. & Mirkin, C. A. Spherical Nucleic Acids. *Journal of the American Chemical Society* **134**, 1376-1391, doi:10.1021/ja209351u (2012).

97 Koo, K. M., Sina, A. A. I., Carrascosa, L. G., Shiddiky, M. J. A. & Trau, M. DNA–bare gold affinity interactions: mechanism and applications in biosensing. *Analytical Methods* **7**, 7042-7054, doi:10.1039/C5AY01479D (2015).

98 Kimura-Suda, H., Petrovykh, D. Y., Tarlov, M. J. & Whitman, L. J. Base-Dependent Competitive Adsorption of Single-Stranded DNA on Gold. *Journal of the American Chemical Society* **125**, 9014-9015, doi:10.1021/ja035756n (2003).

99 Jiang, H., Materon, E. M., Sotomayor, M. D. P. T. & Liu, J. Fast assembly of non-thiolated DNA on gold surface at lower pH. *Journal of Colloid and Interface Science* **411**, 92-97, (2013).

100 Zhang, X., Servos, M. R. & Liu, J. Surface Science of DNA Adsorption onto Citrate-Capped Gold Nanoparticles. *Langmuir* **28**, 3896-3902, doi:10.1021/la205036p (2012).

101 Piana, S. & Bilic, A. The Nature of the Adsorption of Nucleobases on the Gold [111] Surface. *The Journal of Physical Chemistry B* **110**, 23467-23471, doi:10.1021/jp064438i (2006).

102 Bieri, M. & Bürgi, T. Adsorption kinetics of l-glutathione on gold and structural changes during self-assembly: an in situ ATR-IR and QCM study. *Physical Chemistry Chemical Physics* **8**, 513-520, doi:10.1039/B511146C (2006).

103 Bieri, M. & Bürgi, T. l-Glutathione Chemisorption on Gold and Acid/Base Induced Structural Changes: A PM-IRRAS and Time-Resolved in Situ ATR-IR Spectroscopic Study. *Langmuir* **21**, 1354-1363, doi:10.1021/la047735s (2005).

104 Watson, J. D. & Crick, F. H. C. Molecular Structure of Nucleic Acids: A Structure for Deoxyribose Nucleic Acid. *Nature* **171**, 737-738, doi:10.1038/171737a0 (1953).

105 Zhou, W., Wang, F., Ding, J. & Liu, J. Tandem Phosphorothioate Modifications for DNA Adsorption Strength and Polarity Control on Gold Nanoparticles. *ACS Applied Materials & Interfaces* **6**, 14795-14800, doi:10.1021/am504791b (2014).

106 Storhoff, J. J., Elghanian, R., Mirkin, C. A. & Letsinger, R. L. Sequence-Dependent Stability of DNA-Modified Gold Nanoparticles. *Langmuir* **18**, 6666-6670, doi:10.1021/la0202428 (2002).

107 Rothemund, P. W. K. Folding DNA to create nanoscale shapes and patterns.

Nature **440**, 297-302, doi:10.1038/nature04586 (2006).

108 Mastroianni, A. J., Claridge, S. A. & Alivisatos, A. P. Pyramidal and Chiral Groupings of Gold Nanocrystals Assembled Using DNA Scaffolds. *Journal of the American Chemical Society* **131**, 8455-8459, doi:10.1021/ja808570g (2009).

109 Liu, J. & Lu, Y. Smart Nanomaterials Responsive to Multiple Chemical Stimuli with Controllable Cooperativity. *Advanced Materials* **18** (2006).

110 Bowman, M.-C. *et al.* Inhibition of HIV Fusion with Multivalent Gold Nanoparticles. *Journal of the American Chemical Society* **130**, 6896-6897, doi:10.1021/ja710321g (2008).

111 Zheng, D., Seferos, D. S., Giljohann, D. A., Patel, P. C. & Mirkin, C. A. Aptamer Nano-flares for Molecular Detection in Living Cells. *Nano Letters* **9**, 3258-3261, doi:10.1021/nl901517b (2009).

국문 초록

나노스케일의 입자가 가지는 형태는 입자의 특성으로 직결되기 때문에 금속 나노 구조의 형태를 제어하는 것은 것은 매우 중요하다. 이처럼 기하학적 형태에 따라 금속 나노구조의 광학 성질이 변하게 되는 것은 국소 표면 플라즈몬 공명 현상에 기인한다. 표면 플라즈몬이란 전기장에 의해 금속 박막 표면의 전자들이 집단적으로 진동하는 현상이다. 이 때 입사광에 의해 표면 플라즈몬 파가 형성되어 경계면을 따라 일정한 주기로 진행하게 되는 것을 표면 플라즈몬 공명이라고 한다. 금속이 박막이 아니라 입사광의 파장보다 작은 나노 사이즈가 되는 나노 구조체의 경우에는, 전파하는 특성이 아니라 구조체 내에 속박되어 진동하는 특성을 가지게 되는데 이를 국소 표면 플라즈몬 공명이라고 한다. 이러한 국소 표면 플라즈몬 공명 현상에 의해, 금이나 은 같은 귀금속 금속의 경우 그 공명 파장대가 가시광 영역에 존재하며 이는 특정한 색의 빛과 강하게 상호작용할 수 있음을 의미한다. 또한, 플라즈모닉 나노 구조체 인근에서 전자기장이 증폭될 수 있다. 구조체에 인접할수록 전자기장 신호가 커지며, 구조체의 형태에 따라 증폭 정도가 달라질 수 있다. 이 특성은 플라즈모닉 나노입자가 다양한 분야에서 활용성을 가지도록 한다. 이와 같은 흥미로운 광학적 특성 및 응용 특성으로 인해 나노 구조체의 형태를 제어하고자 하는 많은 노력이 있어왔다. 씨앗 매개 성장

합성법은 바텀 업 방식 중 하나인 금속 이온 환원법을 통한 대표적인 플라즈모닉 나노구조체 제조 방법으로, 핵 생성 단계와 입자 성장 단계를 분리함으로써 구조체의 크기와 형태를 제어하는 것이 용이한 방법이다. 이를 이용하여 다양한 형태를 가진 나노 구조체들이 보고되었으나, 그 방법과 얻을 수 있는 모양이 제한적이었다. 본 연구를 통하여 우리는 기존의 나노 구조체 제조법의 한계를 넘고자 하였다. 기존에 보고되지 않았던 형태의 플라즈모닉 나노 구조체를 제조하는 새로운 방법에 대하여 연구하였으며, 이렇게 합성된 나노 구조체들의 광학 특성 평가를 진행했다. 먼저 본 연구에서는 유기 티올 분자를 나노입자의 씨앗 매개 성장에 첨가함으로써 나노파티클의 성장을 조절할 수 있는 새로운 합성법을 이용 하였다. 일반적으로 유기 티올 분자는 나노입자 표면에 작용기를 도입하고 이를 이용한 어셈블리를 할 때 이용된다. 본 연구에서는 형태 제어에 있어 유기 티올 분자의 새로운 역할을 재조명 하였으며 독특한 형태와 광학 특성을 가지는 기존에 보고되지 않은 새로운 나노입자를 제조하였다. 본 연구에서는 또한 핵산 분자를 금나노입자의 씨앗 매개 성장 합성 과정에 도입하여 카이랄성을 지닌 나노 구조체를 제조하였으며 기존 보고되었던 카이랄 나노입자의 특성을 제어하였다. 핵산 분자 내의 오탄당 구조는 카이랄 탄소를 보유하고 있으며 핵산 분자 내의 염기구조는 금 표면과 상호작용할 수 있기 때문에 핵산 분자 고유의 구

조적 특성과 금나노입자의 광학적 특성을 효과적으로 결합한 카이랄 금나노입자를 합성할 수 있었다. 특히, 흥미롭게도 단일 가닥 DNA의 염기 서열에 따라, 합성된 나노입자의 카이랄성이 다양하게 변화함을 확인할 수 있었다. 이는 정교한 프로그래밍을 통한 다양한 패턴화된 핵산 서열을 나노 구조체 합성 과정에 이용함을 통해 결과물 나노입자의 카이랄성을 다양하게 제어하고, 또 증대할 수 있음을 의미한다.

주요어: 플라즈몬, 나노입자, 형상, 라만 산란, 카이랄성, 핵산

학번: 2014-21431